SANDIA REPORT
SAND2021-14876
Printed November 2021

Complementary Study of Radiative Heat Transfer and Flow Physics from Moderate-scale Hydrocarbon Pool Fire Simulations

Jared R. Kirsch, Joshua A. Hubbard

Prepared by
Sandia National Laboratories
Albuquerque, New Mexico
87185 and Livermore,
California 94550

Issued by Sandia National Laboratories, operated for the United States Department of Energy by National Technology & Engineering Solutions of Sandia, LLC.

Available to DOE and DOE contractors from
U.S. Department of Energy
Office of Scientific and Technical Information
P.O. Box 62
Oak Ridge, TN 37831

Telephone: (865) 576-8401
Facsimile: (865) 576-5728
E-Mail: reports@osti.gov
Online ordering: http://www.osti.gov/scitech

Available to the public from
U.S. Department of Commerce
National Technical Information Service
5301 Shawnee Rd
Alexandria, VA 22312

Telephone: (800) 553-6847
Facsimile: (703) 605-6900
E-Mail: orders@ntis.gov
Online order: https://classic.ntis.gov/help/order-methods/

ABSTRACT

As part of the Advanced Simulation and Computing Verification and Validation (ASCVV) program, a 0.3-m diameter hydrocarbon pool fire with multiple fuels was modeled and simulated. In the study described in this report, systematic examination was performed on the radiation model used in a series of coupled Fuego/Nalu simulations. A calibration study was done with a medium-scale methanol pool fire and the effect of calibration traced throughout the radiation model. This analysis provided a more detailed understanding of the effect of radiation model parameters on each other and on other quantities in the simulations. Heptane simulation results were also examined using this approach and possible areas for further improvement of the models were identified. The effect of soot on radiative losses was examined by comparing heptane and methanol results.

CONTENTS

LIST OF FIGURES

LIST OF TABLES

This page left blank

EXECUTIVE SUMMARY

Sandia National Laboratories has developed computational tools for modeling and simulation of important weapons environments, including pool fires which occur in accident scenarios. The primary code used for low-Mach, turbulent reacting flow modeling is known as SIERRA/Fuego, and has been in use for over 15 years [1]. As part of the Advanced Simulation and Computing Verification and Validation program, a 0.3 m diameter hydrocarbon pool fire with multiple fuels was simulated using the Multiple-Program-Multiple-Data coupling of SIERRA/Fuego and Nalu to perform computational fluid dynamics turbulence modeling as well as radiation modeling. The Fuego combustion model was a Strained Laminar Flamelet Model, and the radiation model was a Participating Media Radiation Model which used a gray-gas assumption. The primary objective of the project was the comparison of turbulence statistics, fluxes, and radiative heat loss metrics from the simulations with those from a robust set of experiments in order to validate the Sandia-developed code in pool fire applications.

Two fuels were modeled in order to examine the effects of soot formation on radiative heat loss, with the first fuel modeled being methanol (non-sooting), and the second heptane (sooting). This report outlines work done to support the primary project objective. A calibration study was performed on the radiation model with methanol as the fuel. The radiation model was examined from initial quantities queried from the flamelet libraries to the characteristic radiative heat loss quantity – the radiant fraction. This analysis provided insight into the dependence of each key quantity in the radiation model upon the preceding quantities, and provided a clearer view of why varying the radiation model parameters worked to modify the radiant fraction. For the heptane fires, the radiation model analysis provided insight into the effect of parameters including soot quantities queried from the flamelet library on the radiant fraction. Integral quantities describing important flow physics were computed using ParaView/Python and other quantities were reported along the domain centerline. A preliminary analysis of the effect of soot on radiative losses was performed by comparing heptane and methanol results.

Additional analyses for methanol included an analysis showing the sensitivity of the flame height computed using an intermittency definition to the value of the chosen threshold variable. A brief comparison of coarse and fine data was also done, and the effect of mesh resolution on the subgrid and total turbulent kinetic energy was analyzed.

This work was important in providing radiation model calibration in non-sooting flames where gas radiation was dominant. In addition, it provided insight into the SIERRA/Fuego and Nalu models and the flow and heat transfer physics occurring in the simulated pool fires. The most important results are summarized in the list below.

- The radiative intensity, scalar flux, and enthalpy sink term $\partial q_i^r / \partial x_i$ increased with increasing absorption and radiation source magnitudes. Consequently, plume radiant fraction increased and plume temperature decreased.

- Prefactors (f_μ, f_e) used to modify radiation model parameters (absorption coefficient and radiative source) were varied from (0.5, 0.25) to (1, 1) in order to calibrate the model to predict the experimentally reported radiant fraction. The predicted values of plume radiant fraction varied from 0.14 to 0.35 over this range of prefactors.
- The "volumetric flux of buoyant force per volume" (integrated buoyancy flux) increased with increasing temperature. Maximum values varied from 0.39 N/s to 0.47 N/s over the range of parameters considered for the prescribed mass flux boundary condition.
- The rate of change of mass entrainment rate with height increased sharply at the pan lip. The mass entrainment rate increased with height to the vertical domain extent. At the experimentally-derived flame height (0.5 m), the entrainment rate varied from 0.119 kg/s to 0.122 kg/s for the range of parameters considered for the prescribed mass flux boundary condition. The simulation case yielding the closest radiant fraction to the experimental value predicted a mass entrainment rate of 0.12 kg/s at the mean flame height, and a Society of Fire Protection Engineers (SFPE) correlation yielded a value of 0.09 kg/s. The simulation results were likely higher than the SFPE correlation due to the fact that the pan was elevated, which caused higher entrainment rates compared to a floor-level pan. In addition, the lip height and the general nature of the correlation could have contributed to this difference.
- Mesh refinement had a noticeable impact on centerline temperature, density, axial velocity, and subgrid turbulent kinetic energy as well as the radiant fraction, integrated buoyancy flux, and mass entrainment rate. However, the effect on radiative heat flux and radiant fraction was not significant enough to necessitate the use of the finer mesh (less than 5% difference for both quantities).
- Flame height was estimated using an engineering correlation and the importance of correctly predicting the mass flux on the pool surface was shown.
- A sensitivity study showed that the computed flame height is sensitive to the value of the threshold temperature or mixture fraction used when computing flame height with an intermittency definition.
- Soot production appeared to be under-predicted in 30cm heptane fires. Further development of the soot formation mechanism modeled may be necessary.
- The heptane results were compared to the best case methanol results and were shown to exhibit higher radiative heat transfer. Because the contribution of soot to radiation was insignificant, the predicted gas phase radiation was the primary contributor to this increased radiation.

ACRONYMS AND DEFINITIONS

Abbreviation	Definition
SNL	Sandia National Laboratories
ASC	Advanced Simulation and Computing
ASCVV	Advanced Simulation and Computing Verification & and Validation
MPMD	Multiple-Program-Multiple-Data
CFD	Computational Fluid Dynamics
LES	Large Eddy Simulation
PMR	Participating Media Radiation
SLFM	Strained Laminar Flamelet Model
QOI	Quantity of Interest
BRTE	Boltzmann Radiative Transport Equation
ID	Inside Diameter
BC	Boundary Condition
TKE	Turbulent Kinetic Energy

1. INTRODUCTION

The Advanced Simulation and Computing (ASC) program at Sandia is a part of the NNSA mission which involves simulation and computing work aimed toward extension of nuclear weapon lifetimes in the stockpile. Verification and Validation (V&V) program activities include the creation of standards, methods, and metrics for assessing model credibility and quantifying confidence in simulation results. Also included in V&V activities are assessments which establish credibility and confidence for specific simulations [2]. The objective of this project was to build credibility in pool fire modeling capabilities with the second-generation Sandia National Laboratories physics and chemistry models. Verification and validation of moderate-scale, non-sooting hydrocarbon pool fires was done in the primary thrust of the project [3]. This report details a complementary analysis which was done to calibrate the computational models, analyze the radiation model, compare simulations of sooting and non-sooting fuels, and examine radiative heat transfer and fluid dynamics from a series of simulations.

1.1. Objectives

The work summarized in this report represents analysis complementary to the primary project objective (modeling and simulation & verification and validation of flow statistics). The main objectives detailed in this report are as follows.

- Report integral quantities such as radiant fraction in order to inform the simulation process
- Analyze radiation model used in the fire simulations. Specifically, examine the effect of inputs to the radiative transport equation or soot evolution equations on Quantities of Interest (QOIs). For methanol, this was done in the form of a calibration study with the absorption coefficient and radiative source term as inputs and integral QOIs (esp. radiant fraction) as primary outputs. For heptane, this was done by examining soot source terms as well as the absorption coefficient and radiative source term from a heptane flamelet library with a heptane boiling point boundary condition.
- Compute and report integral flow quantities describing entrainment and buoyancy
- Analyze computed flame height from engineering correlation in light of multiple boundary conditions used
- Perform sensitivity study examining the effect of threshold temperature or mixture fraction value chosen for calculation of flame height using intermittency definition
- Compare results for methanol and heptane to examine the effect of soot on radiative heat transfer

1.2. Related Studies

1.2.1. Methanol

The 30 – 31-cm diameter methanol pool fire is a specific validation case of the International Association for Fire Safety Science (IAFSS) Working Group on Measurement and Computation of Fire Phenomena (MaCFP Working Group). This moderate-scale methanol pool fire has been well characterized experimentally, with several detailed studies being reported in [4-11]. The fires were characterized with measurements of velocity and temperature, fluxes of heat and mass, chemical composition, and other quantities. In particular, Weckman [4] conducted one of the earliest studies on the fire at the University of Waterloo. This study provided a velocity and temperature dataset containing mean and RMS values, length scales, turbulence intensity, and correlations. In addition, the description of experimental setup, entrainment phenomena, and other flow characteristics provided valuable background to the current study.

The National Institute of Standards and Technology published results from several experimental studies which provided temperature, velocity, mass and heat flux, radiant fraction, soot mass and volume fractions, and other data [7, 8, 10]. The experimentally expected value of radiant fraction for a 30-cm diameter methanol pool fire was found to be 0.22 ± 0.02. Falkenstein-Smith et al. performed a study in which gas species measurements were reported to characterize the chemical structure of a moderate-scale methanol pool fire. These measurements helped to describe the factors driving the radiative heat feedback to the pool surface [6]. Klassen and Gore [12] reported the radiative heat loss fraction, flame height, fuel mass burning rate, and radiative heat flux, among other quantities. Kim et al. measured radiative and total heat flux and calculated convective heat flux. They showed that radiation was the dominant mechanism of heat feedback to the fuel surface, accounting for 67% to 88% of the total heat feedback. The enthalpy convected in the plume was also found to represent a dominant fraction of the fire's total energy, 68% to 75% [9].

In addition to experimental studies for this methanol fire, several computational studies have been conducted. Ma et al. [13] used a second-order iterative variable-density pressure-based low-Mach number solver developed in-house to perform an LES simulation of the fire. The default configuration of an elevated pan with a 1-cm lip above the fuel surface was modeled. Other configurations included an elevated pan with no lip and a floor-flush pan with no lip. The entrainment and overall flow pattern were found to be significantly affected by the presence of a pan lip, whereas the pan elevation did not have as strong of an effect. The effect of a lip was noted in an earlier study by Orloff and De Ris [14], and the results match qualitatively, considering the difference in fuel used. Important simulation results included puffing frequency, mean and RMS temperature and velocity, mean molar fractions, radiative loss, and radiative and total heat feedback to the fuel surface.

Ahmed and Trove [15] used FireFOAM to model and simulate the fire and utilized two radiation modeling methods: 1) a prescribed global radiant fraction and 2) a model based on the Weighted-Sum-of-Gray-Gases approach. A mesh sensitivity study yielded the spatial resolution necessary to achieve grid-converged solutions in the region near the fuel surface and in the bulk flow region. Mean and RMS temperature and velocity, mean radiative and convective heat fluxes near the pool surface, and overall flow behavior were also reported.

1.2.2. Heptane

Several relevant heptane pool fire experiments have also been conducted. Raj and Prabhu [16] characterized heptane pool fires with a range of diameters including 0.3-m and reported the mass burning rate and radiative fraction. They also noted that a non-zero lip height modified entrainment, and thus, convective and radiative heat fluxes. By examining the instantaneous mass burning rate over time, they distinguished an initial steady state fuel mass flux and a bulk boiling period fuel mass flux. Temperature, soot volume fraction, and radiative heat fluxes for a 0.3-m diameter heptane pool fire were reported by Klassen and Gore [12] among other quantities. In this study, methanol was used as a representative alcohol and heptane as a representative paraffin. They found that the radiative heat flux incident on the fuel surface was more dependent on diameter for methanol fires than for heptane fires. The fires examined always exhibited strong radiative heat feedback and no diameter corresponded to a convective regime. Hamins et al. [17] developed a method for estimating the radiative heat loss fraction via a single point measurement and found it to be accurate to within 13% of a multilocation measurement. They noted that radiative heat feedback to the pool surface controls the fuel burning rate. Koseki and Hayasaka [18] examined the scale dependency of heptane fire properties and compared results for simple model predictions of temperature, radiant fraction, and other quantities to experimental data. Kang et al. [19] conducted an experimental study on heptane pool fires from 0.1 to 0.3 m in diameter. They identified four typical burning phases for pool fires of this size, which they described as 1) pre-burning, 2) quasi-steady state burning, 3) boiling burning, and 4) decaying. The second and third phases correspond to those mentioned by Raj and Prahbu. Flame height, burning rate, and temperature vs. time for the fuel surface and wall were reported. It was noted that boiling burning will occur when the wall temperature is greater than or equal to the fuel boiling point. Chen et al. [20] also studied thin-layer heptane pool fires and noted the distinct phases which Kang et al. described. Additionally, they noted the effect of the fuel thickness on the flame height and burning rate. Evaporation was enhanced during boiling. The formation of bubbles and effect on the heat absorbed by the fuel surface were observed. Kamiuto et al. [21] characterized the soot contents of flames for several fuels including heptane. They used a constrained multispectral transmittance method to determine *in situ* soot size distributions and volume fractions.

Kang et al. [22] conducted an early computational study on a 5.7-cm diameter hexane pool fire which used an LES turbulence model with Smagorinsky eddy viscosity model for subgrid-scale (SGS) closure. A modified laminar flamelet model (MLFM) was used to model combustion and was compared to a simple mixture fraction model. Flame structure was examined and the MLFM was shown to improve predictions of temperature and velocity vs. those made with the mixture fraction model. Chatterjee et al. [23] simulated a 30-cm heptane pool fire with the fuel surface elevated by 0.15 m from the ground and a prescribed mass flux boundary condition. The turbulence modeling scheme was LES and the subgrid soot-radiation model was based on the laminar smoke point concept. They compared experimental results for temperature, velocity, soot volume fraction, and fuel surface heat flux to experimental results, with reasonable accuracy shown in their numerical predictions. Wu et al. [24] performed a detailed computational study of a 7.1-cm diameter heptane pool fire in which a Monte Carlo ray tracing-based radiation solver with spectral models for five gas species and soot was used. Soot was modeled using a two-equation soot evolution model with C_2H_2-based inception. Velocity, temperature, radiative heat flux, soot volume fraction, and other results were presented. The spectral radiation model was an advancement in complexity compared to other works which used the grey-gas model and was believed to improve the predictions of radiative quantities. Radiative quantities were found to be very sensitive to the soot volume fraction.

2. THEORY

Pool fire radiation was modeled as Participating Media Radiation (PMR) in Nalu. Such a model was necessary because gas and soot both participate in radiative heat transfer by absorbing and emitting radiation. In the following subsections, the coupling of Fuego to Nalu, and an overview of the chemistry and physics models used for sooting and non-sooting fires are given. Section 2.4 gives theory related to the plume analysis

2.1. CFD-PMR Program Coupling

SIERRA/Fuego is used for turbulent flow and combustion modeling, while Nalu is used for radiation modeling. During a simulation, the flamelet library (see Section 3.2) is queried to obtain parameters including the absorption coefficient and radiation source term for the Boltzmann Radiative Transport Equation (BRTE). These parameters – along with the emissivity, transmissivity, and boundary source term – are passed to Nalu for radiation modeling. In Nalu, the radiative source term for the BRTE is used in the equation solve to obtain the radiative intensity $I(s)$, where s_i represents the i^{th} direction and is defined in Figure 2-1 [25]. In this definition, θ_{zn} and θ_{az} are the zenith and azimuthal angles respectively. Nalu proceeds to calculate the radiative flux (q_i^r) and scalar flux (G) and pass them along with the incident flux to Fuego, where they are used in the calculation of the radiative source term for enthalpy transport and other quantities. This coupling is summarized in Figure 2-2.

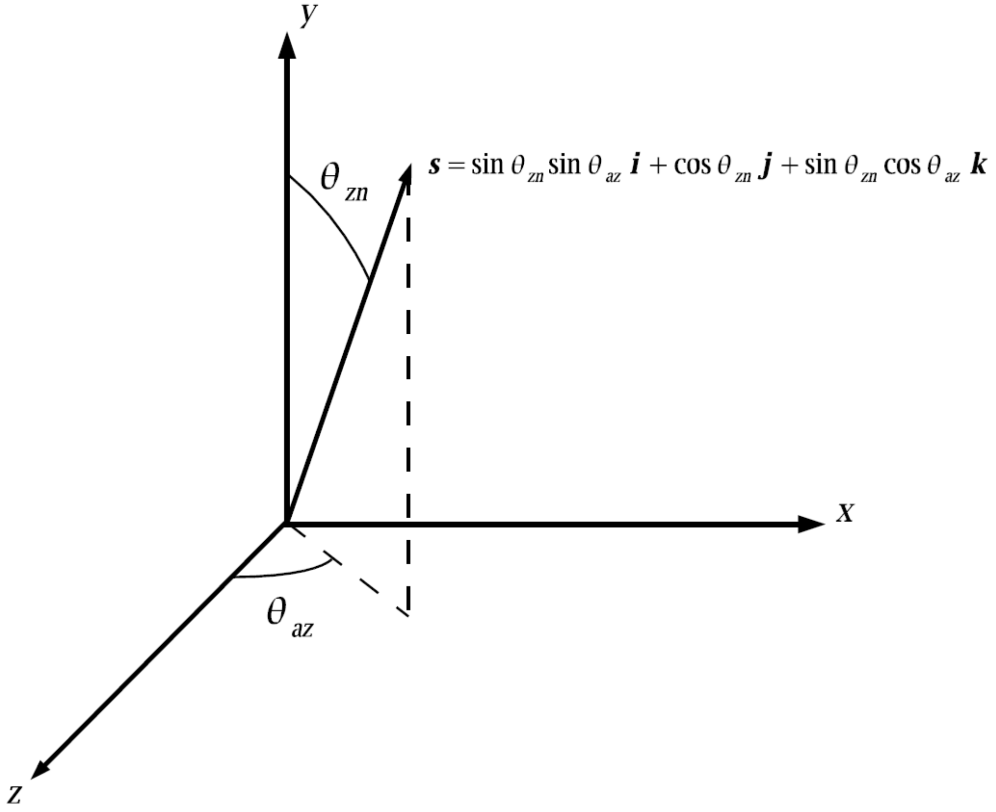

Figure 2-1. Definition of ordinate direction, taken from Fuego Theory Manual [25]

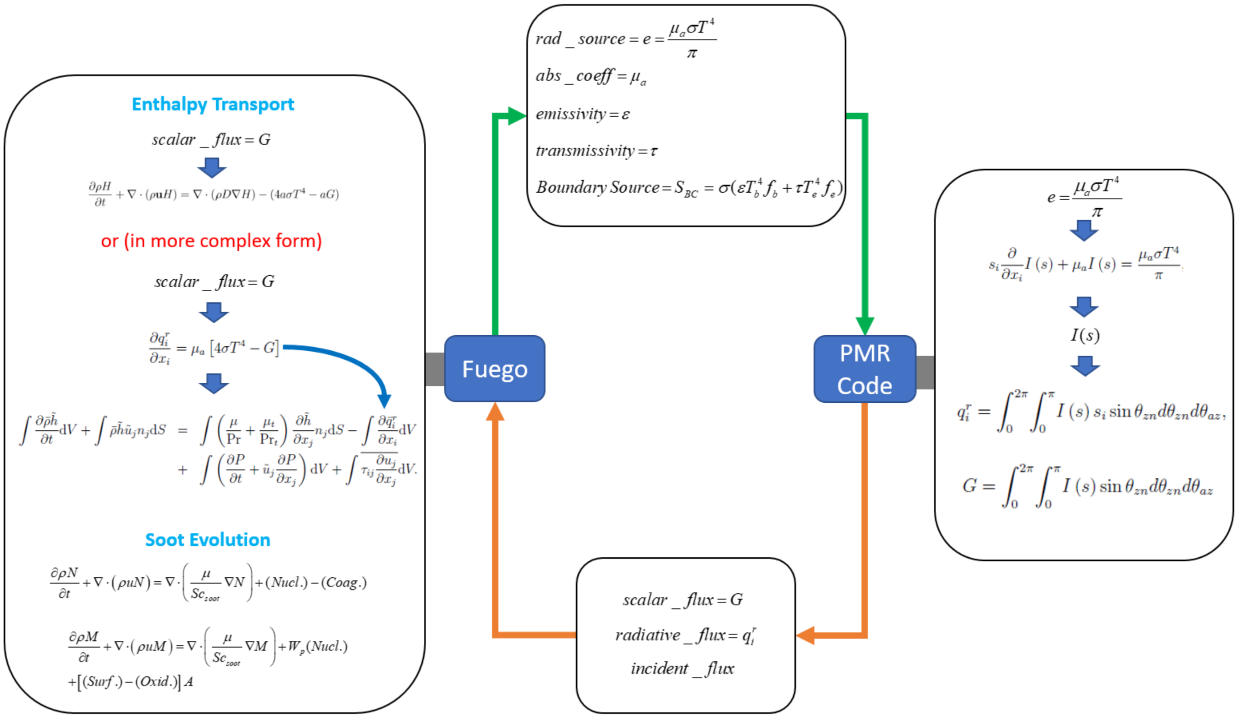

Figure 2-2. Fuego/Nalu coupling

2.2. Radiation Model – Non-sooting Fire

In Figure 2-2, several important quantities and equations relevant to the radiation model are shown. This illustrates the dependencies between Fuego and Nalu. By examining the quantities and equations which lead from parameters such as the absorption coefficient and radiative source term for the BRTE to the integral quantities such as enthalpy deficit flux and radiant fraction, the effect of the model parameters upon the model outputs may be understood. This section gives the quantities and equations leading from the absorption coefficient and radiative source term for the BRTE to the radiant fraction. Plots of these quantities are shown in Section 4.1.1.

Equation (2.1) shows the radiative source term for the BRTE, where μ_a is the absorption coefficient and σ is the Stefan-Boltzmann constant. The absorption coefficient and radiative source term (e_g) for the BRTE are obtained from the flamelet library as mentioned above and passed to Nalu. In Nalu, the radiative source term for the BRTE and the absorption coefficient are used to solve the BRTE (Eq. (2.2)) for the radiative intensity $I(s)$, where s_i represents the i^{th} direction as defined in Figure 2-1.

$$e = e_g = \frac{\mu_a \sigma T^4}{\pi} \tag{2.1}$$

$$s_i \frac{\partial}{\partial x_i} I(s) + \mu_a I(s) = \frac{\mu_a \sigma T^4}{\pi} \tag{2.2}$$

With the radiative intensity calculated, the radiative flux (q_i^r) and scalar flux (G) are determined using Equations (2.3) and (2.4), respectively.

$$q_i^{\,r} = \int_0^{2\pi}\int_0^{\pi} I(s)s_i \sin\theta_{zn} d\theta_{zn} d\theta_{az} \tag{2.3}$$

$$G = \int_0^{2\pi}\int_0^{\pi} I(s)\sin\theta_{zn} d\theta_{zn} d\theta_{az} \tag{2.4}$$

The enthalpy transport equation contains a term which accounts for radiative heat transfer to the control volume, and this source term is computed from the scalar flux using Eq. (2.5). The source term is then used to solve for enthalpy in Eq. (2.6).

$$\frac{\partial q_i^{\,r}}{\partial x_i} = \mu_a[4\sigma T^4 - G] \tag{2.5}$$

In Equation (2.6), $\bar{\rho}$ is the spatially-filtered fluid density, $\tilde{h}$ is the Favre-averaged enthalpy, $\tilde{u}_j$ is the jth component of Favre-averaged velocity, n_i is the unit normal vector component in the x_i direction, V is the computational cell volume, S is the length variable along the integration path, μ is the viscosity, μ_t is the modeled subgrid turbulent eddy viscosity from momentum closure, Pr is the Prandtl number, Pr_t is the turbulent Prandtl number, $\bar{q}_i^r$ is the spatially-filtered radiative flux, P is the pressure, and τ_{ij} is the viscous stress tensor.

$$\begin{aligned}\int \frac{\partial \bar{\rho} h}{\partial t} dV + \int \bar{\rho} h u_j n_j dS = \int \left(\frac{\mu}{\mathrm{Pr}} + \frac{\mu_t}{\mathrm{Pr}_t} \right) \frac{\partial h}{\partial x_j} n_j dS - \int \frac{\partial \bar{q}_i^{\,r}}{\partial x_i} dV \\ + \int \left(\frac{\partial P}{\partial t} + u_j \frac{\partial P}{\partial x_j} \right) dV + \int \overline{\tau_{ij} \frac{\partial u_j}{\partial x_j}} dV\end{aligned} \tag{2.6}$$

With the simulation complete, the reported variables are used to form the enthalpy deficit integrated flux as shown in Eq. (2.7) and the mixture fraction integrated flux as in Eq. (2.8). Finally, the radiant fraction is formed as in Eq. (2.9).

$$\text{Enthalpy Deficit Integrated Flux} = \gamma'' = \int_0^{\infty} \rho u[h - h_{ad}(Z)]rdr \tag{2.7}$$

$$\text{Mixture Fraction Integrated Flux} = Z'' = \int_0^{\infty} uZ\rho rdr \tag{2.8}$$

$$\text{Radiant Fraction} = X_r = \frac{\gamma''}{Z'' h_C} \tag{2.9}$$

2.3. Radiation Model – Sooting Fire

This section gives the important additional equations in the modeling of a sooting fire such as heptane. Because the presence of soot can affect radiative heat transfer significantly [26], the starting point for the radiation model used in the heptane simulations is soot evolution. To include soot in the model, a two-equation soot model is implemented in Fuego, in which transport of both the number density (ρN) and mass concentration (ρM) are considered in the development of soot. The transport equations are given by Eqns. (2.10) and (2.11) below, and take several source terms from the flamelet library as inputs. These equations are described in [27], including the definitions of the soot Schmidt number ($\mathrm{Sc_{soot}}$), soot nucleate molecular weight (W_p), and total surface area (A).

Along with the gas absorption coefficient ($\mu_{a,g}$) and gas radiative source term (e_g) for the BRTE, the soot absorption coefficient ($\mu_{a,s}$) and soot radiative source term (e_s) are also obtained from the library along with source terms for soot evolution equations. The nucleation source term, $nucleation\_source$, is denoted by $(Nucl.)$, $coagulation\_source$ by $(Coag.)$, $surface\_growth\_source$ by $(Surf.)$, and $oxidation\_source = o2\_oxidation\_source + oh\_oxidation\_source$ by $(Oxid.)$. The equations are then solved in Fuego to obtain the soot number density (ρN) and soot mass concentration (ρM) [27]. The soot number of moles per mass (N) and soot mass fraction (M) are computed from the soot number density and soot mass concentration, respectively, where ρ is the total density in the cell. The soot mass fraction is used in the computation of the absorption coefficient (Eq. (2.12)), which is a combination of the gas absorption coefficient $\mu_{a,g}$ and the soot absorption coefficient $\mu_{a,s}$. It is also used to form the radiative source term (Eq. (2.13)) for the Boltzmann Radiative Transport Equation (Eq. (2.14)), and this source term also contains contributions from both gas and soot.

$$\frac{\partial \rho N}{\partial t} + \nabla \cdot \left(\rho u N\right) = \nabla \cdot \left(\frac{\mu}{\mathrm{Sc_{soot}}} \nabla N \right) + (Nucl.) - (Coag.) \tag{2.10}$$

$$\frac{\partial \rho M}{\partial t} + \nabla \cdot \left(\rho u M\right) = \nabla \cdot \left(\frac{\mu}{\mathrm{Sc_{soot}}} \nabla M \right) + W_p (Nucl.) + \left[(Surf.) - (Oxid.)\right] A \tag{2.11}$$

$$\text{absorption coefficient} = \mu_a = \mu_{a,g} + M \mu_{a,s} \tag{2.12}$$

$$e = e_g + M e_s = \frac{\mu_{a,g} \sigma T^4}{\pi} + M \frac{\mu_{a,s} \sigma T^4}{\pi} \tag{2.13}$$

$$s_i \frac{\partial}{\partial x_i} I(s) + \mu_a I(s) = e \tag{2.14}$$

From Equation (2.14) on, the important quantities and equations follow as shown in the previous section, eventually leading to the radiant fraction. In Figure 2-2, this corresponds to the computation of radiative intensity, scalar flux, and radiative flux in the box by "PMR Code" followed by the transfer to Fuego (orange arrows) and subsequent computations in it.

2.4. Plume Analysis

2.4.1. Entrainment Rate

Additional plume physics besides radiation were also analyzed in this study. Quantities describing these physics included entrainment rate, integrated buoyancy flux, and flame height. The momentum flux was also computed for heptane. These quantities as well as radiation model quantities were post-processed using ParaView/Python.

The entrainment rate in the plume is calculated as the vertical mass flow rate in the plume (Eq. (2.15)) and is taken to be equivalent to the mass flow rate at which air enters the plume. This is justified due to conservation of mass and the fact that the mass flow rate contributed by the fire source is small relative to the mass flow rate of the air in the plume [28].

$$m_{ent} = \int 2\pi \overline{u\rho}\, r dr \tag{2.15}$$

Entrainment rate can also be estimated using engineering correlations given in the Society of Fire Protection Engineers (SFPE) Handbook of Fire Protection Engineering [28]. Eqns. (2.16) - (2.18) give these correlations, where Eqn. (2.16) is used below the mean flame height, Eqn. (2.17) is used at the mean flame height, and Eqn. (2.18) is used above the mean flame height. In Eqns. (2.16) - (2.18), z is the distance above the pool surface in meters, z_0 is the virtual origin computed as in Eqn. (2.19) (Eqn. 13.32 in [28]), $\dot{Q}_c$ is the convective heat release rate calculated as shown in Eqn. (2.20), and L is the mean flame height in meters (see Section 4.1.7 for information on flame height). In the present study, $\dot{Q}_c$ is approximately 16.6 kW, L is 0.5 m, and D is 0.3 m.

$$\dot{m}_{ent}(kg/s) = 0.0058\dot{Q}_c(kW)\cdot\frac{z}{L} \tag{2.16}$$

$$\dot{m}_{ent,L}(kg/s) = 0.0058\dot{Q}_c(kW) \tag{2.17}$$

$$\dot{m}_{ent}(kg/s) = 0.071\dot{Q}_c^{1/3}(z-z_0)^{5/3}\cdot\left[1+0.027\dot{Q}_c^{2/3}(z-z_0)^{-5/3}\right] \tag{2.18}$$

$$\frac{z_0}{D} = -1.02 + 0.083\frac{\dot{Q}^{2/5}}{D} \tag{2.19}$$

$$\dot{Q}_C = (1 - X_R)\dot{Q} = (1 - X_R)\dot{m}_f H_C \tag{2.20}$$

In the development of these formulas, data from Zukoski and Cetegen were used [29, 30], which were from experiments using 0.19 – 0.5-m diameter pans with and without surrounding floors. The effect of pan lip height was not mentioned, but the effect of the floor was significant for the 0.5-m diameter burner. The absence of a floor was said to increase the mass flow by ~30% for this burner.

2.4.2. Integrated Buoyancy Flux

Another integral quantity considered in this work was the integrated buoyancy flux, or buoyancy flow. Delichatsios noted that buoyancy is a very important phenomenon in pool fires, as it provides the energy for the formation of large eddies which entrain ambient air and mix it with fuel [31]. The integrated buoyancy flux computed in this study was defined by Delichatsios as in Equation (2.21) and represents the overall integrated buoyancy flux in the plume caused by increased temperature and subsequently lower density. He also provided a formula for estimation of the integrated buoyancy flux at the flame tip, which is given in Equation (2.23). In this equation, g is the acceleration due to gravity, $\dot{Q}$ is the total heat release rate, X_A is the combustion efficiency, X_R is the radiant fraction, C_p is the specific heat of the gases, and T_∞ is the ambient temperature.

$$B(Z) = g\int 2\pi \overline{ru(\rho_\infty - \rho)}\, dr = g\iint_{\theta r} \overline{u(\rho_\infty - \rho)}\, r\,dr\,d\theta = g\int_A \overline{u(\rho_\infty - \rho)}\, dA \tag{2.21}$$

$$\begin{aligned} &\int \frac{\partial \bar{\rho}\tilde{u}_i}{\partial t} dV + \int \bar{\rho}\tilde{u}_i\tilde{u}_j n_j dS + \int \left(\bar{p} + \frac{2}{3}\bar{\rho}q^2 \right) n_i dS = \\ &\qquad \int 2\left(\mu + \mu_t\right)\left(\tilde{S}_{ij} - \frac{1}{3}\tilde{S}_{kk}\delta_{ij} \right) n_j dS + \int \left(\bar{\rho} - \rho_0\right) g_i dV \end{aligned} \tag{2.22}$$

$$B_\infty = \frac{g\dot{Q}(X_A - X_R)}{C_p T_\infty} \tag{2.23}$$

The integrated buoyancy flux is related to the buoyant source term in the momentum conservation equation of the LES turbulent flow model used in this study (last term in Eqn. (2.22)). However, in the integrated buoyancy flux, the density deficit is multiplied by axial velocity before averaging and integrating. Because the buoyant source term in Eqn. (2.22) is the buoyant force which contributes to the momentum in the plume, the integrated buoyancy flux has the appearance of a "volumetric flow of buoyant force per volume", or the rate of change of buoyant force per unit time.

2.4.3. Flame Height

In pool fires, pan diameter is an important parameter of the pool geometry. A distinguishing geometric feature of the resulting flame is the flame height. Typically, the flame height is reported as the height to which the visible flame extends. Engineering correlations exist for the estimation of flame height [28]. When flame height is reported from experiments, it is often taken as the height at which the intermittency is 50% [28]. Intermittency is defined as the fraction of time for which a point in space at a certain elevation contains part of the flame.

A common engineering correlation [32] used for estimation of mean flame height is given in the SFPE Handbook of Fire Protection Engineering (Eq. (2.24) below). In this relationship, L is the mean flame height in meters, D is the pan diameter in meters, and $\dot{Q} = \dot{m}_f H_c$ is the total heat release rate in kW, where $\dot{m}_f$ is the fuel mass burning rate in kg/s and H_c is the lower heat of combustion of the fuel in kJ/kg.

$$L = -1.02D + 0.235\dot{Q}^{2/5} \tag{2.24}$$

3. SIMULATION DESCRIPTION

3.1. Pool Fire Scenarios

Two fuel types were examined in this study – methanol and heptane. Methanol was chosen due to the robust body of experimental work which exists for this fuel in moderate-scale pool fires and the fact that it is a fuel which does not produce soot during combustion, thus simplifying the modeling approach. Heptane was chosen as a fuel which produces soot. Sooting flames are more representative of the thermal environments relevant to abnormal thermal environment analysis.

The geometry of the pool fires was derived from experiments [4, 12] and is given below in Figure 3-1 and Figure 3-2. The characteristic dimension of the pan is the diameter, which was 30 cm, and the rim/lip height, another significant dimension, was 1 cm. The domain extents were chosen so as to allow for a realistic solution out to ambient conditions.

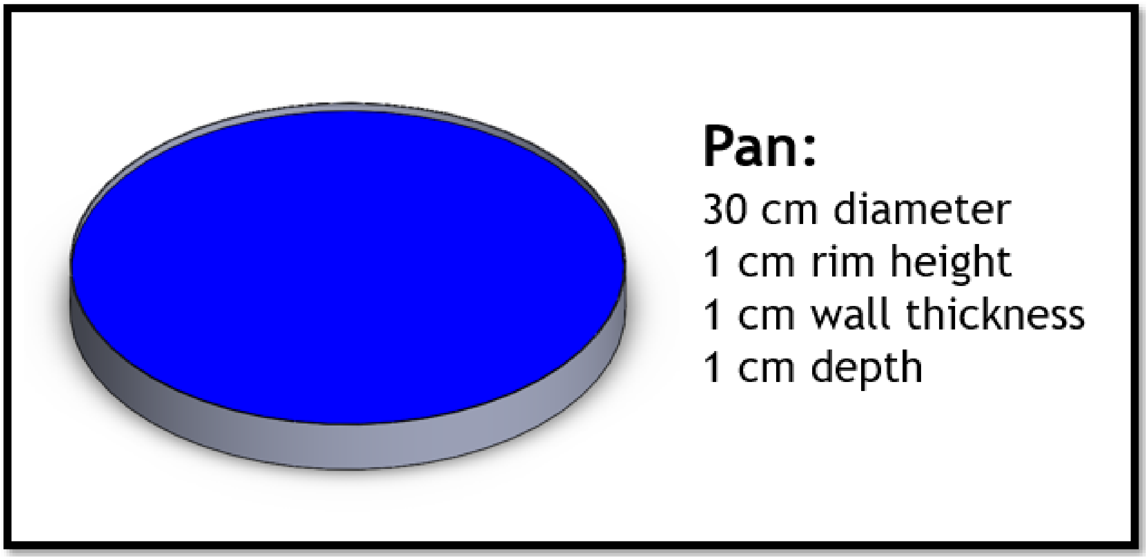

Figure 3-1. Pan dimensions

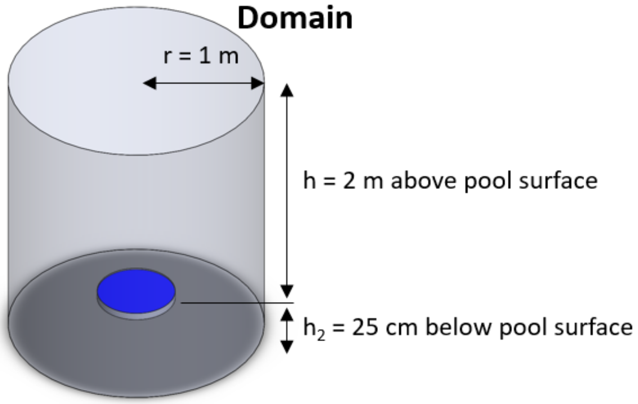

Figure 3-2. Domain dimensions

3.2. Modeling and Simulation Information

Sandia National Laboratories (SNL) developed a low-Mach module for simulation of turbulent reacting flow, specifically as the primary element in the ASC fire environment simulation project [25]. This module of the SIERRA code suite is known as Fuego, and represents the turbulent, buoyantly-driven incompressible flow, heat transfer, mass transfer, combustion, soot, and absorption coefficient model portion of the simulation software. Using Multiple-Program-Multiple-Data (MPMD) coupling, Fuego is coupled to Nalu for Participating Media Radiation (PMR) modeling.

Fuego has multiple options for turbulence modeling and, in this project, a Large Eddy Simulation (LES) scheme was used, with closure being provided by a subgrid scale kinetic energy one-equation (or *K sgs*) closure model. LES uses spatial filtering and was chosen due to the fact that it produced time-varying results which were essential for calculation of statistics necessary for comparison with experimental data.

Turbulent combustion modeling was performed in Fuego using a Strained Laminar Flamelet Model (SLFM), in which turbulent flames are treated as an ensemble of laminar diffusion flames, and nonequilibrium chemistry is included by accounting for localized fluid strain. By resolving chemical scales in the phase space of the mixture fraction instead of a 3D grid, computational efficiency is improved [25]. Chemistry is assumed to occur only in a thin layer around stoichiometry and to be quasi-steady on the scale of the flow. Thus, the chemical structure in mixture fraction space is pre-computed and the resulting table is queried during the simulation to obtain flow properties. More details about the modeling scheme for the methanol simulations can be found in Hubbard et. al. [3].

The heptane flamelet library was recently computed based on a modified version of the model presented by Aksit and Moss [33]. Soot was modeled using a two-equation soot model as described in Section 2.3.

Methanol simulations were run with two mesh sizes and the results examined to determine the effect of mesh refinement on key quantities in the solution (Section 4.1.5). The coarser mesh was determined to yield acceptable results, and thus, heptane simulations were only conducted with the coarser mesh resolution.

4. RESULTS AND ANALYSIS

4.1. Methanol

The methanol pool fires documented in this report closely followed the experimental setup of Weckman [4], with the 0.3-m ID pan being elevated such that the fuel surface was 0.25 m above the floor.

An optically-thin gray-gas assumption was used in the formation of the library's absorption properties. Using this assumption results in an under-prediction of the reabsorption of radiant emissions and an over-prediction of the radiant heat emitted by the flame [3]. To address this problem without increasing computational cost by using a more accurate gas radiation model, prefactors were used to decrease the gas absorption coefficient and radiation source term queried from the library. Figure 4-1 shows this strategy: parameters were queried from the library, multiplied by prefactors, and then used in the radiative transport equation. By iterating through a series of prefactors, the predicted radiant fraction was adjusted to the experimentally expected value. Thus, a model calibration study was performed which calibrated the radiation model for this fire to predict a radiant heat loss fraction which agreed with experimental data.

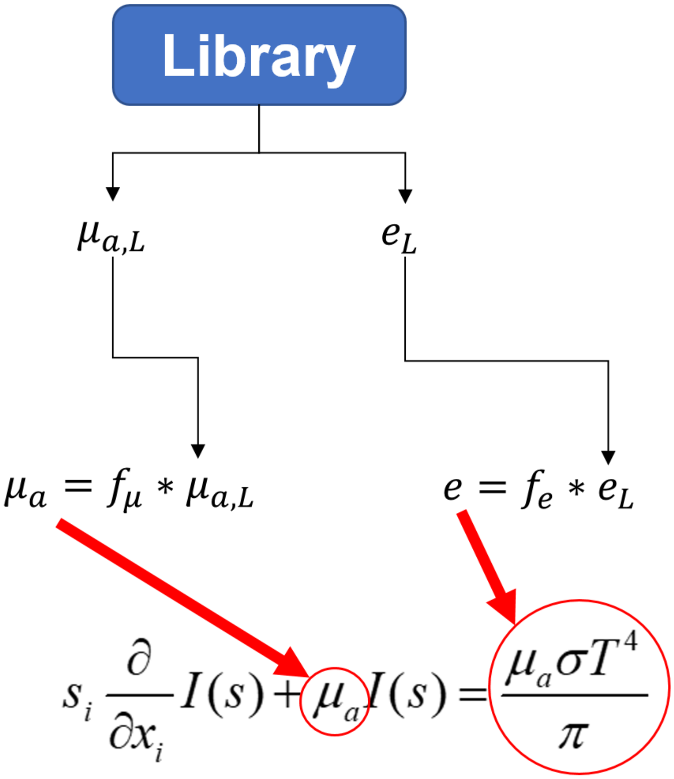

Figure 4-1. Use of prefactors to modify inputs to BRTE

The results in the following two sections are thus presented in the form of a calibration study (and in a sense, a sensitivity study), where multiple cases representing the series of prefactors are shown on each plot. Thus, the effect of the prefactors on the quantity shown can be seen.

Besides using multiple sets of prefactors, two different types of boundary conditions were used. The first was a mass flux boundary condition in which the mass flux on the pool surface was prescribed (denoted "mass flux BC"), and the second was a pool boundary condition, in which parameters for a pool evaporation model were specified and a heat and mass transfer balance problem was solved. The pool boundary condition resulted in a significantly underpredicted mass flux in most cases. One of the ramifications of low mass flux predictions is discussed in the calculation of flame height from an engineering relation.

In Section 4.1.1, only the mass flux BC cases and the pool BC case in which the predicted mass flux agreed with experimental values are presented. This is done in order to clearly show the effect of the prefactors on important quantities in the radiation model. All cases, including both boundary conditions are presented in Appendix A.

In Section 4.1.5, a brief comparison of data produced on a coarse mesh with data produced on a fine mesh is presented, for the case which was found to most accurately predict the radiant fraction.

Finally, Section 4.1.7 gives results for flame height estimation using an engineering correlation. It also includes a sensitivity study relating the flame height computed using an intermittency definition to threshold variables used to define the flame tip. This study shows that the threshold value used for the calculation of flame height is important and must be chosen carefully. This section also uses only the data from the case which most accurately predicted the radiant fraction.

Table 4-1 gives an overview of the simulation cases including the boundary condition on the pool surface and the radiation model prefactors. All cases used the gray-gas model.

Table 4-1. Overview of simulation cases by boundary condition and prefactors

Pool Surface BC	Mesh Resolution	Gas Absorption Coefficient Multiplier	Gas Radiation Source Multiplier
Prescribed mass flux	coarse	0.5	0.25
Prescribed mass flux	fine	0.5	0.25
Prescribed mass flux	coarse	0.7	0.4
Prescribed mass flux	fine	0.7	0.4
Prescribed mass flux	coarse	0.75	0.5
Prescribed mass flux	fine	0.75	0.5
Prescribed mass flux	coarse	1	1
Prescribed mass flux	fine	1	1
Predicted mass flux	coarse	0.5	0.25
Predicted mass flux	fine	0.5	0.25
Predicted mass flux	coarse	0.7	0.4
Predicted mass flux	fine	0.7	0.4
Predicted mass flux	coarse	0.75	0.5
Predicted mass flux	fine	0.75	0.5
Predicted mass flux	coarse	1	1
Predicted mass flux	fine	1	1

4.1.1. Radiation Model Framework

During the simulation, Fuego queries the flamelet library to obtain the absorption coefficient (for methanol, this is simply the gas absorption coefficient) and radiative source term for the BRTE. In the study discussed in this section, these parameters were then each multiplied by a prefactor as discussed above to modify the amount of radiative heat transfer in the model. This was important to calibrate the radiation model to experimental data. The prefactors could be different for other fuels.

The plot of absorption coefficient vs. height (Figure 4-2a) clearly shows the effect of multiplication by the prefactor, as the displayed absorption coefficient curves rank in magnitude from that corresponding to the prefactor of 0.5 to those corresponding to the prefactor of 1. Thus, the trend seen in the absorption coefficient is as expected. Because the prefactors for the radiative source term increase as the prefactors for the absorption coefficient increase, the source term was expected to show the same trend. This trend is summarized in Figure 4-3, where the prefactor sets were implemented in the following order: no prefactors, set 0, set 1, and set 2.

Figure 4-2b shows the radiative source (e) term for the BRTE. The curves generally follow the same trend in magnitude as the absorption coefficient curves do. This source term peaks at $z \approx 0.2$ m. In Figure 4-2c, the vector magnitude of the radiative flux along the domain centerline is plotted for all cases. Figure 4-2d gives insight into this quantity for the case with prefactors of (0.75, 0.5) and shows that the vertical component dominates. This is expected since it is the axis of symmetry. This component crosses zero at $z \approx 0.14$ m, near the peak in the centerline temperature. Such a trend can be explained by considering that at each point below the maximum temperature along the centerline, radiation is emitted and absorbed, but since the amount of radiation emitted increases with temperature, there is always a net downward radiative flux due to higher contributions from points above than below. The argument is reversed for points above the point at which the maximum temperature occurs. It should be noted that the zero-crossing of the z-component of radiative flux does not occur exactly where the temperature is maximum, but this could be due to the average vertical contributions to radiative flux from the surrounding area being greater below the point of maximum temperature than above.

The radiative flux magnitude for the "best" simulation case at the pool surface is 13.0 kW/m^2, whereas the NIST reported value is approximately 14.8 kW/m^2 [12].

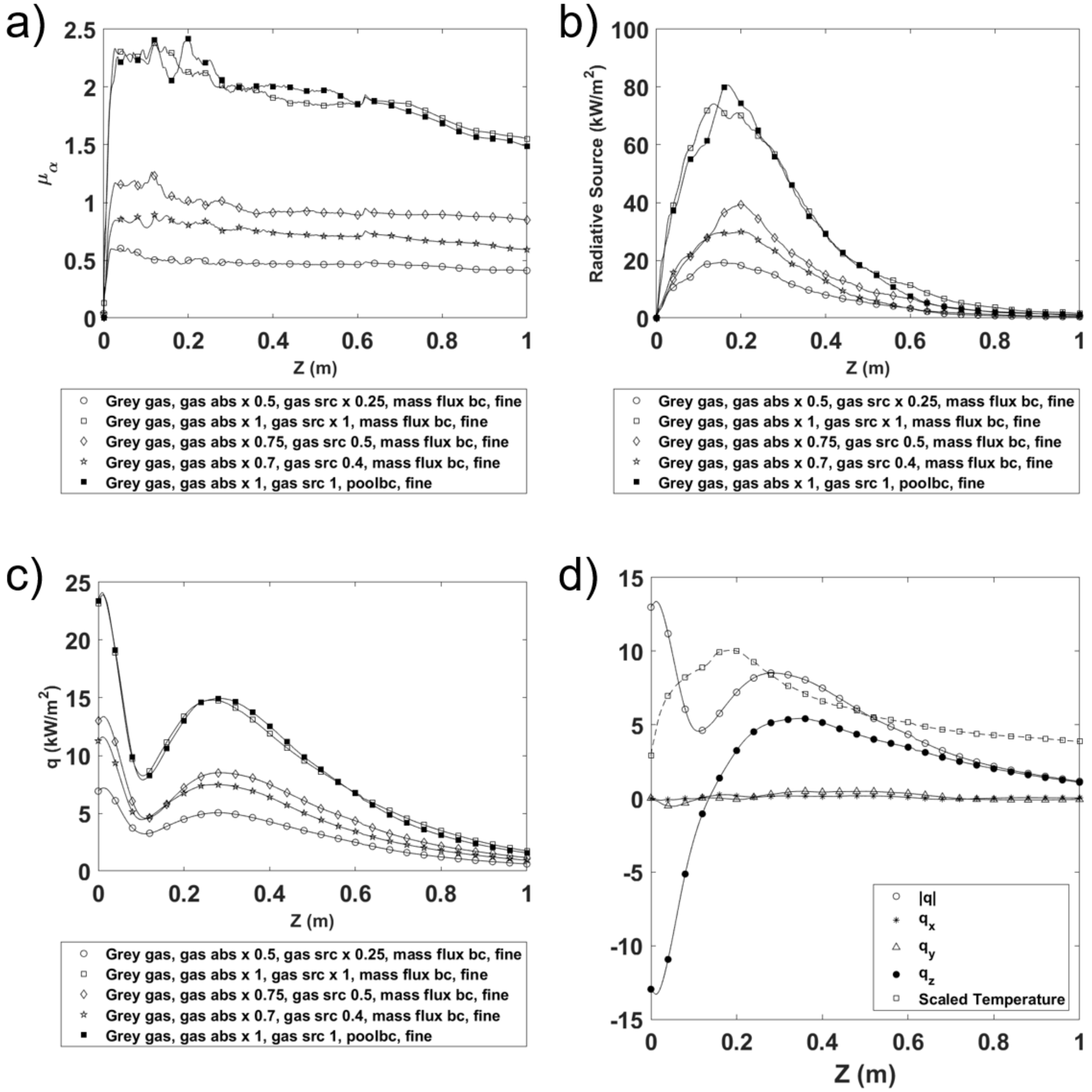

Figure 4-2. a) Absorption coefficient. b) Radiative source term for Boltzmann Radiative Transport Equation. c) Radiative flux vector magnitude. d) Radiative flux vector components and magnitude as well as scaled temperature for reference. All quantities are along domain centerline.

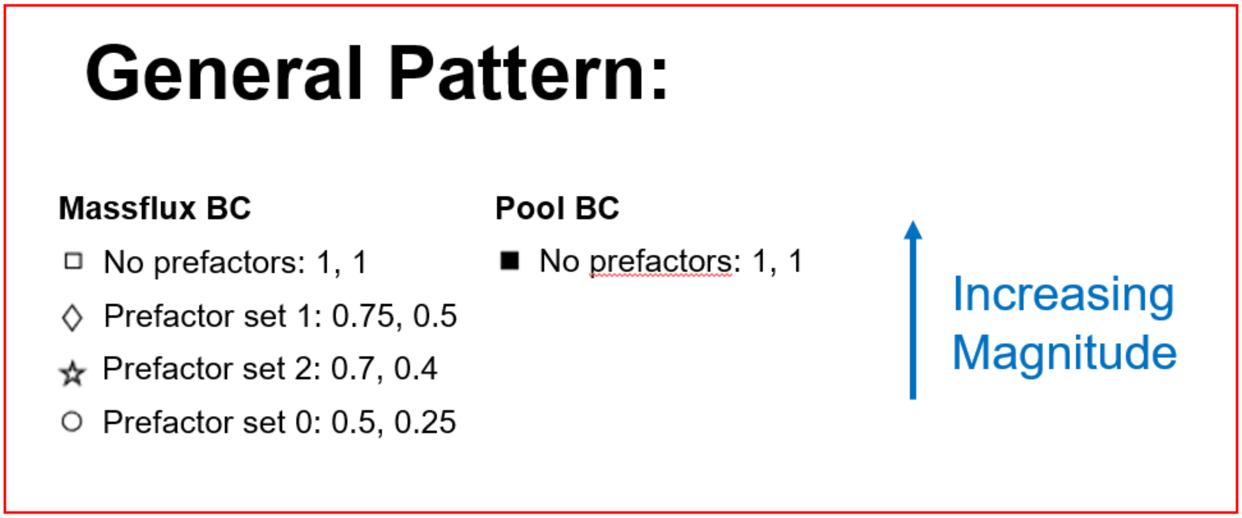

General Pattern:

Massflux BC

- □ No prefactors: 1, 1
- ◇ Prefactor set 1: 0.75, 0.5
- ☆ Prefactor set 2: 0.7, 0.4
- ○ Prefactor set 0: 0.5, 0.25

Pool BC

- ■ No prefactors: 1, 1

Figure 4-3. General magnitude pattern in important radiation model quantities

The scalar flux, Figure 4-4a, is computed in Nalu and sent to Fuego, and clearly reflects the order of the absorption coefficient and radiative source term prefactors. This suggests that higher initial parameters (μ_a and e) lead to a higher radiative intensity from the Boltzmann Radiative Transport Equation. A higher radiative intensity, in turn, produces higher radiative and scalar fluxes.

Figure 4-4b shows the enthalpy sink term, with the pattern shown in Figure 4-3 being visible. This term is the radiative sink term for the enthalpy transport equation, a quantity which describes the enthalpy reduction due to radiative losses. Cases which have higher scalar flux also exhibit a higher enthalpy sink term. This is not necessarily intuitive since scalar flux is subtracted in the source term. Figure 4-4c shows that the emission and absorption terms (sans the absorption coefficient) do not in fact display the trend from Figure 7. However, Figure 4-4d shows that the absorption coefficient has a strong effect on the enthalpy sink term and reorders the cases according to the prefactor magnitude.

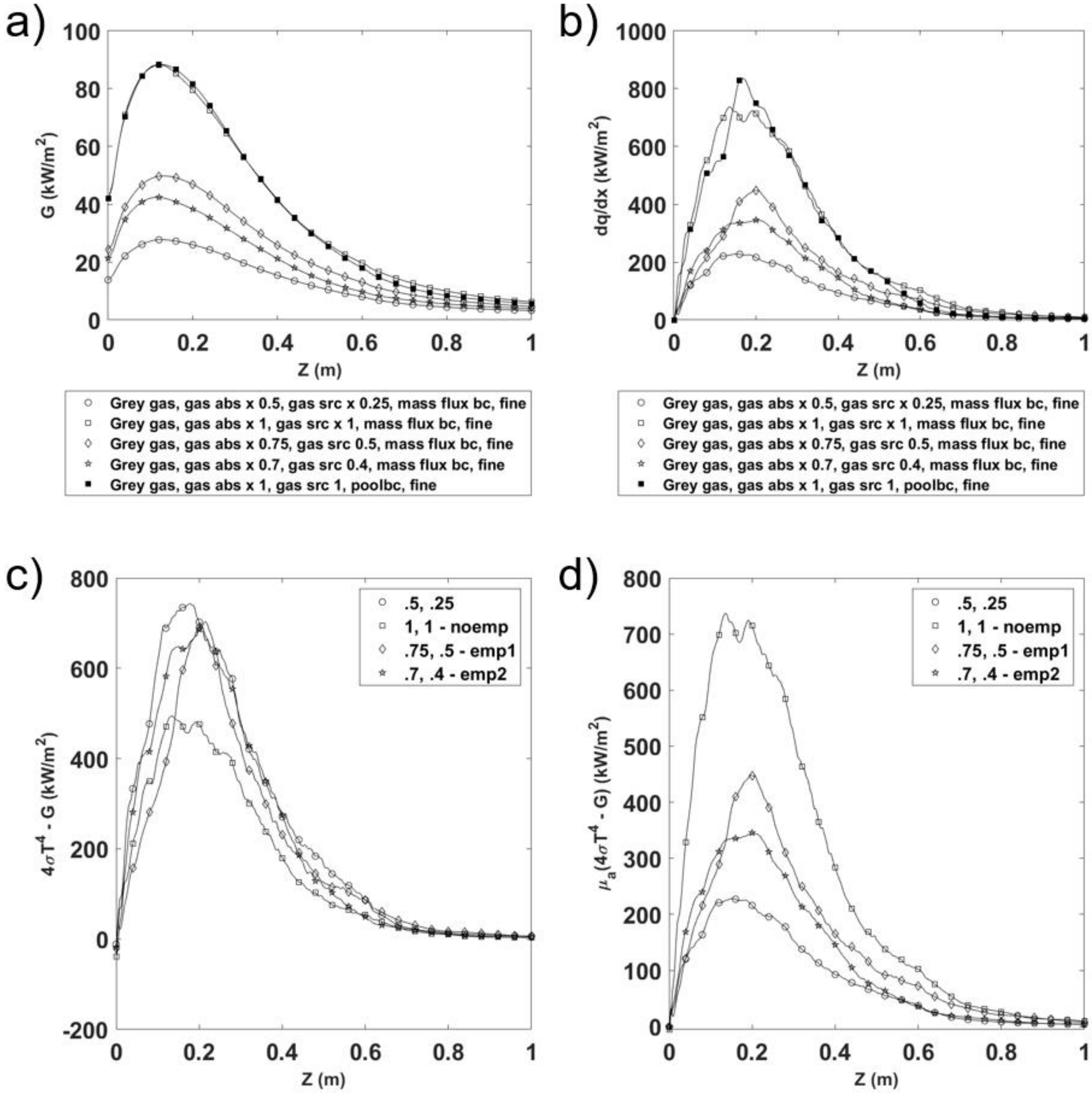

Figure 4-4. a) Scalar flux. b) Radiative sink term for enthalpy transport equation (enthalpy sink term). c) Difference of enthalpy sink terms neglecting absorption coefficient. d) Plot of enthalpy sink term showing the effect of the absorption coefficient for the prescribed mass flux BC cases. All quantities are along domain centerline.

Integrated enthalpy deficit flux (γ'') magnitude is the numerator of the radiant fraction and is shown in Figure 4-5. The trend of increasing magnitude with increasing prefactors on the radiative flux parameters is clearly seen, and the difference in magnitude from case to case is relatively large. The mixture fraction flux (Z'', Figure 4-5) is the denominator of the radiant fraction and does not show clear separation between cases. This reflects low dependence of the mixture fraction flux on the radiation model parameters and contrasts with the relatively high dependence on those parameters shown by the integrated enthalpy deficit flux. The trends of the enthalpy deficit flux are thus reflected clearly in the radiant fraction, which is shown in Figure 4-6.

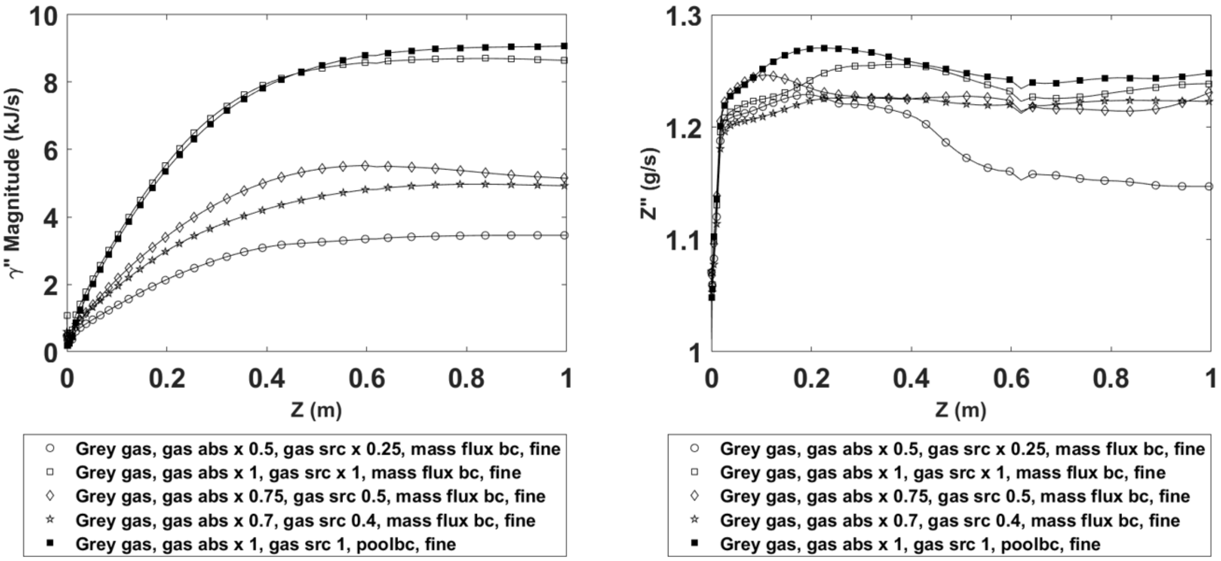

Figure 4-5. Integrated enthalpy deficit flux (left), and integrated mixture fraction flux (right)

The radiant fraction (Figure 4-6) can be thought of as the fraction of the heat of combustion that is lost by the flame through radiation. It increases steadily until around 0.1 m past the mean flame height and then remains relatively constant or drops slowly. The value considered for comparison with experimental data was taken to be the value at $z = 0.6$ m, where most curves achieved their maximum value. The radiant fraction is the end result of the sensitivity study and the primary metric in radiation model calibration. The default gas radiation model parameters (1,1) yielded the curves with a maximum radiant fraction of around 0.35, which is more representative of other flames, e.g., heptane radiant fractions with a mass flux representative of the bulk boiling period [18]. The model was then calibrated by using the prefactors of 0.5, 0.25 with the result being a radiant fraction of around 0.14, which is more typical of hydrogen jet flames [34]. Prefactors of 0.7, 0.4 yielded a radiant fraction of around 0.2, and a final set of prefactors (0.75, 0.5) yielded a value within a satisfactory range of the experimentally predicted radiant fraction (0.22) [4-11]. Plume radiative losses were thus shown to be sensitive to the radiation model parameters. A plot of all simulation cases considered is shown in Appendix A.1

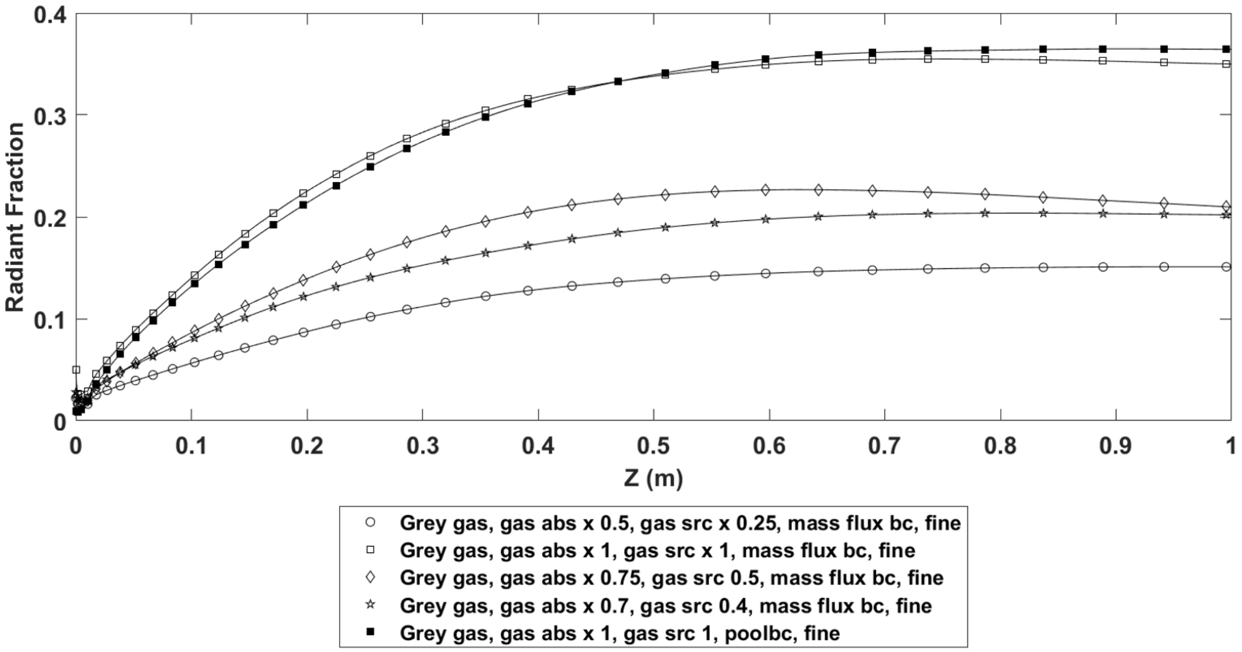

Figure 4-6. Radiant fraction. Time-averaged integral over horizontal planes.

4.1.2. Conclusions from Radiation Model Analysis

In conclusion, it was shown that the radiation model used to simulate a 0.3 m diameter methanol pool fire could be effectively calibrated to predict a realistic radiant fraction by modifying prefactors of the absorption coefficient and radiation source term queried from the flamelet library. Scaling was imposed on the absorption coefficient and radiative source term for the Boltzmann Radiative Transport Equation which effectively modified the strength of plume radiation. This scaling appeared in several quantities throughout the radiation model. By analyzing the important quantities leading from the initial parameters to the radiative fraction, it was seen that the scaling imposed by the prefactors was generally reflected in the quantities analyzed and thus a physical explanation for why each quantity would be higher if the model included stronger radiation was formed. In the PMR gray-gas radiation model used, if the gas absorption coefficient and gas radiation source are increased, the radiative intensity, radiative heat flux, and scalar flux increase. In addition, the radiative sink term in the enthalpy transport equation increases causing a decrease in enthalpy. This causes the integrated enthalpy deficit flux magnitude to be higher, and the radiant fraction is also higher.

4.1.3. Integral Buoyancy Flux and Entrainment Rate

The analysis of the radiation model quantities provides valuable information regarding the effect of the absorption coefficient and radiative source on radiative heat transfer in the flame. These parameters also had a significant effect on buoyancy in the plume due to the fact that higher radiative loss corresponds to lower temperature and lower buoyancy. The effect on entrainment was less noticeable.

Higher absorption coefficient and radiant source values lead to higher radiative intensity, which causes higher scalar flux. The radiation sink term in the enthalpy transport equation is also higher, reflecting larger radiative losses. Larger radiative losses cause lower plume temperatures in general. When the plume is cooler, buoyant acceleration is lower, and this is reflected by a decrease in the integrated buoyancy flux, or volumetric flow of buoyant force per volume (Figure 4-7). The general trend for all cases is that integrated buoyancy flux increases up to a height near the mean flame height and decreases for higher z-values.

The integrated buoyancy flux at the mean flame height was predicted using Delichatsios' formula (Eqn. (2.23)). This value was calculated using the following assumptions: 1) specific heat of gases is the specific heat of air, 2) combustion efficiency is unity, and 3) the total heat release rate is 21.3 kW. The result is shown in Figure 4-7 along with the simulation values. The percent difference between the case with prefactors of (0.75, 0.5), and the Delichatsios' formula, is about 22%. However, agreement would be improved with lower combustion efficiency and heat release rate included in the calculation, so the comparison shown simply illustrates that relatively good agreement with the expected value was achieved.

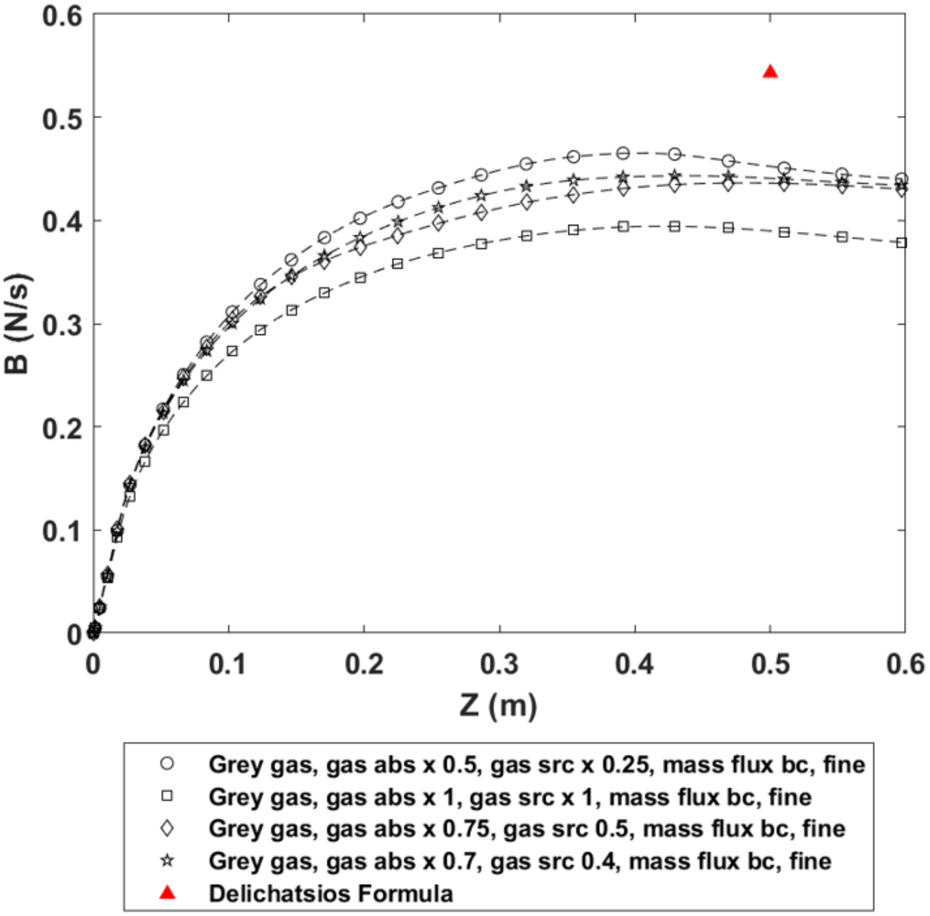

Figure 4-7. Integrated buoyancy flux in plume

Section 2.4.1 includes the mathematical definition and physical description of the entrainment rate. In the calculation of the entrainment rate, the integration limit below the pan lip is the pan internal diameter and above the pan, the integration radius is either the domain radius or is dictated by a mixture fraction threshold.

A filter restricting the radius used for integration was found to be necessary for computation of the entrainment rate. Integration over the domain radius above the pan lip resulted in a large jump in the computed entrainment rate. This sudden increase did not accurately reflect the phenomena occurring in the plume itself, but reflected contributions from a significant area outside of the plume. By increasing the integration radius from the pan radius to the domain radius at the pan lip, many small contributions to the entrainment rate were included from outside of the plume. This is shown by the small arrows with a positive vertical component which are clearly outside of the plume extent in Figure 4-8. Thus, the integration radius was smoothly increased to capture only plume phenomena using a mixture fraction threshold filter in ParaView/Python, with the mixture fraction threshold set to 1e-4. This value was found to accurately represent the plume extent and the resulting integration domain is shown by the colored region of the representative contour plot in Figure 4-9.

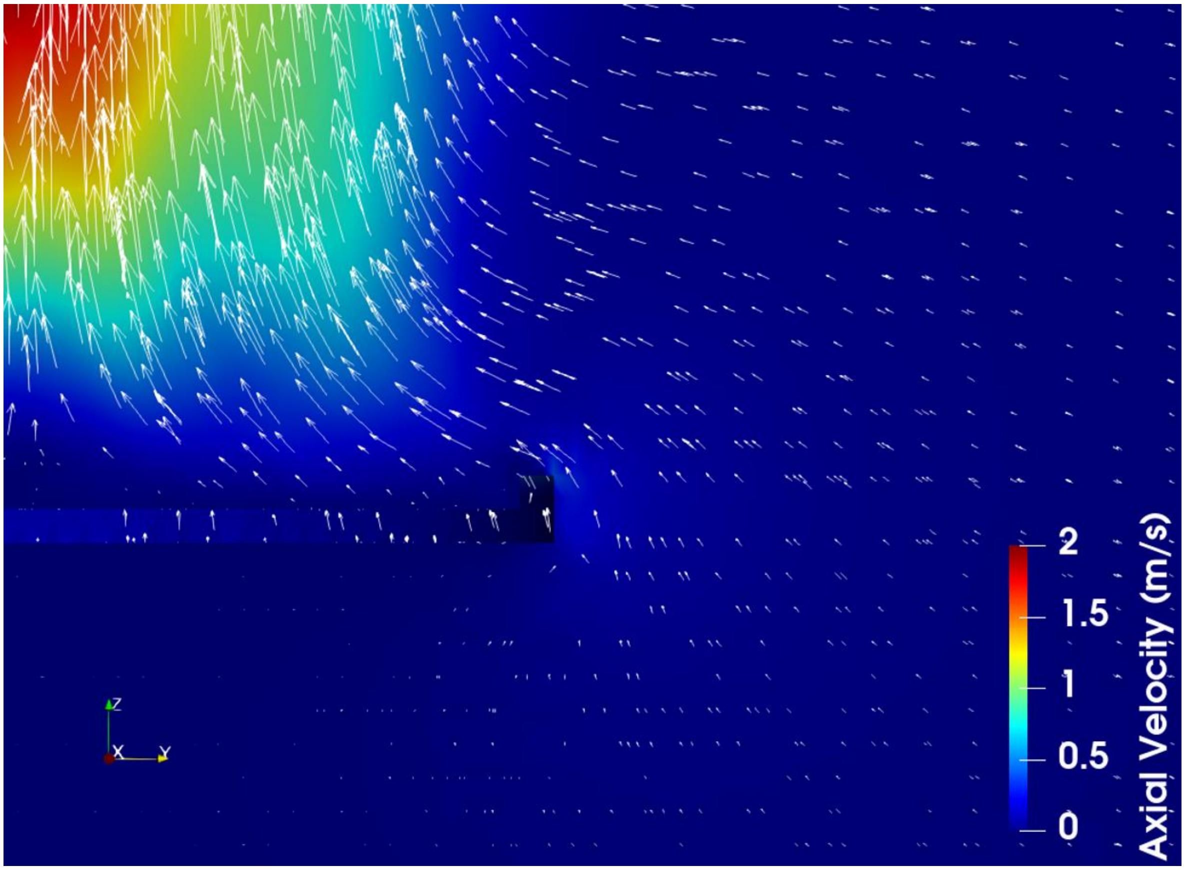

Figure 4-8. Representative velocity contour/glyph plot illustrating near-lip entrainment

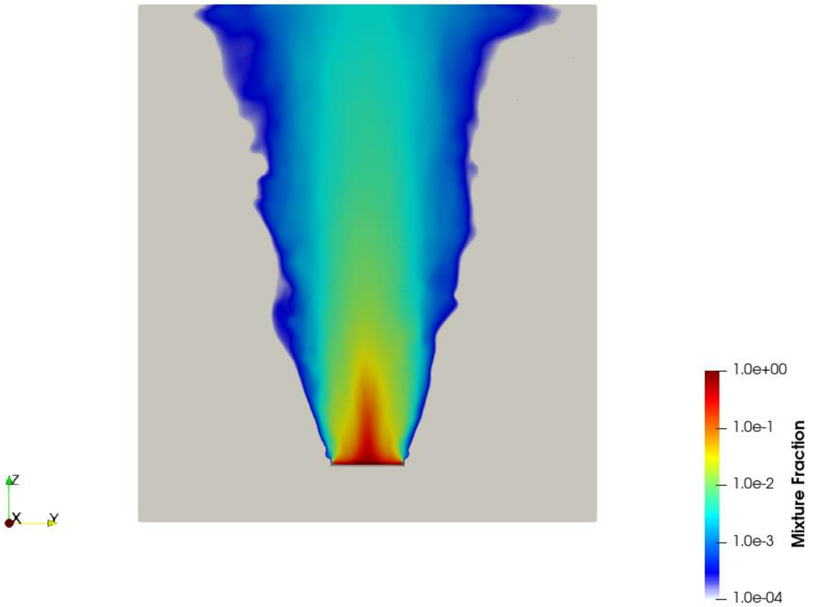

Figure 4-9. Plume extent as defined by mixture fraction filter

The difference in computed entrainment rate as a result of using the mixture fraction filter is shown in Figure 4-10. The threshold results are shown in the top plot and the results from calculations not using a threshold are shown in the bottom plot.

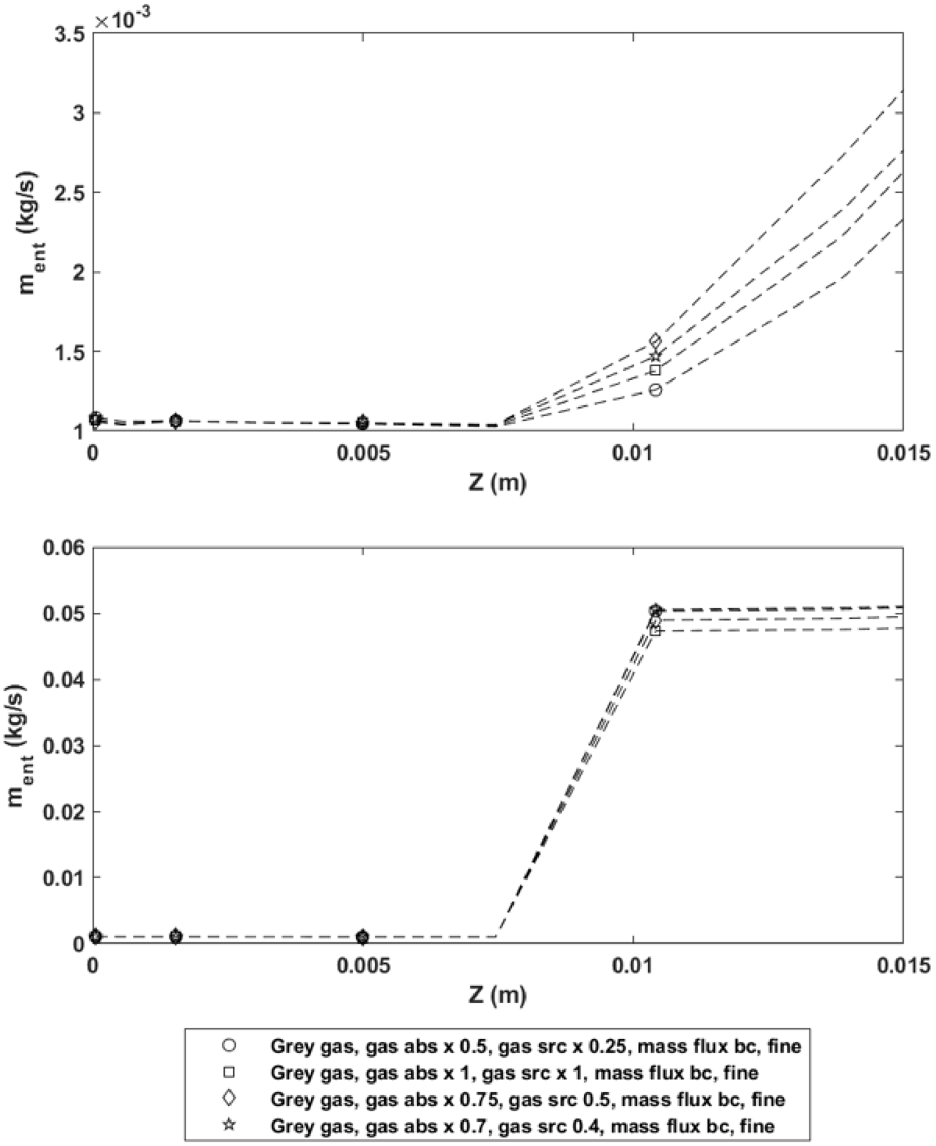

Figure 4-10. Effect of threshold filter on entrainment rate. (Top) entrainment rate computed with the use of a threshold filter. (Bottom) entrainment rate computed without the use of a threshold filter.

The computed entrainment rate from simulation data was compared to engineering correlations given in the SFPE Handbook of Fire Protection Engineering. These equations are given as Eqns. 2.16 – 2.18 in Section 2.4.1. The entrainment rate computed using the threshold is seen to provide better agreement with the engineering relationships than that computed without the threshold, particularly at low heights (Figure 4-11 and Figure 4-12). The simulations performed in this study involved elevated burners (equivalent to the "without floor" experimental results reported by Cetegen [30]), so the simulation data are expected to be higher than the prediction given in the equations above. However, the rapid increase in entrainment rate at the pan lip resulting from an integral taken without the mixture fraction threshold is still believed to give an unrealistic characterization of the entrainment rate in the plume.

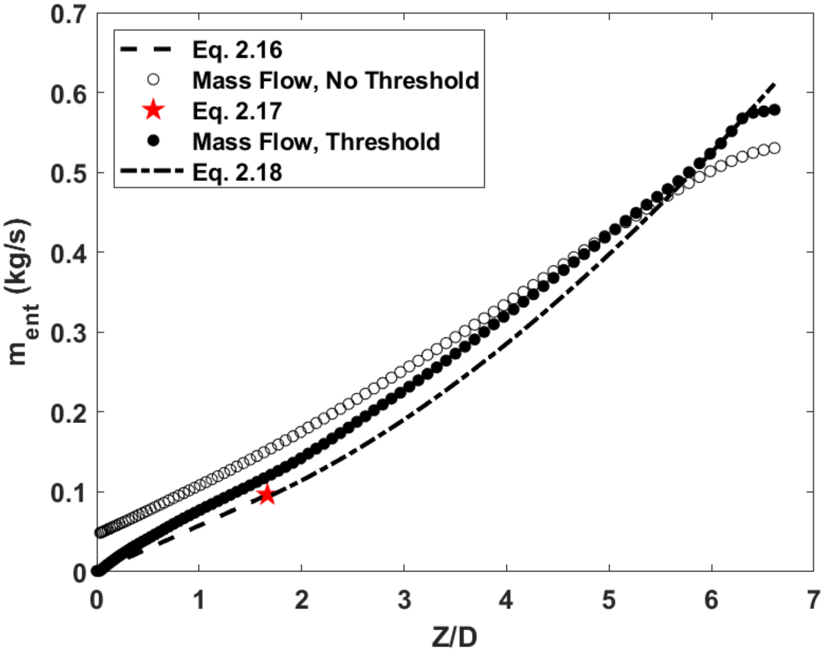

Figure 4-11. Comparison of entrainment rate from simulation to engineering relations

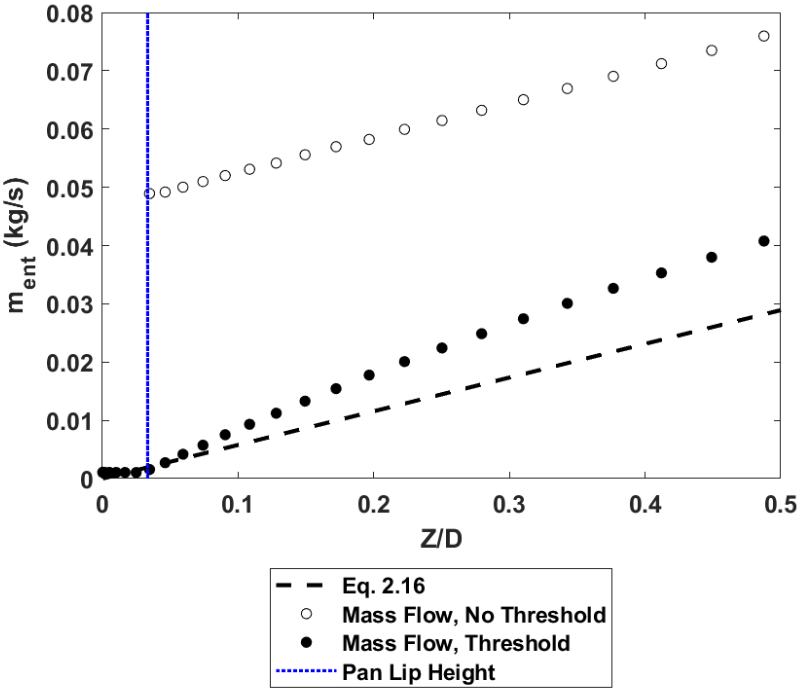

Figure 4-12. Comparison of entrainment rate from simulation to engineering relations, low heights ($z < h \approx 0.16\ m$)

If the entrainment rate is calculated as the rate at which mass flow changes with height, then a sudden increase is noticeable at the pan lip because the slope changes quickly at that height. Thus, the mass flow rate should not change dramatically at the lip, but the rate at which the mass flow changes with height does.

Although air does flow into the plume at a higher rate at the lip, some of the air flows over the lip and downward, some flows strongly inward (radially), some flows up, and much circulates in eddies just above the lip, etc. This supports the notion of an increase in slope ($\partial m_{ent}/\partial z$) rather than a sharp increase in value (m_{ent}) at the pan lip. The plume begins entraining more air at the lip, and that air then participates in combustion, changes in composition, circulates in eddies, rises in temperature, and experiences buoyant acceleration along with fuel and combustion products, etc. These phenomena contribute to a vertical mass flow rate which begins increasing substantially at the pan lip.

Figure 4-13 shows the entrainment rate with a mixture fraction threshold applied for all prefactors and the mass flux boundary condition. The plume entrainment rate remains low and approximately constant in the region below the pan lip, where relatively little air is entrained. At the pan lip, the entrainment rate begins to increase and increases steadily as the vertical velocity and plume diameter increase.

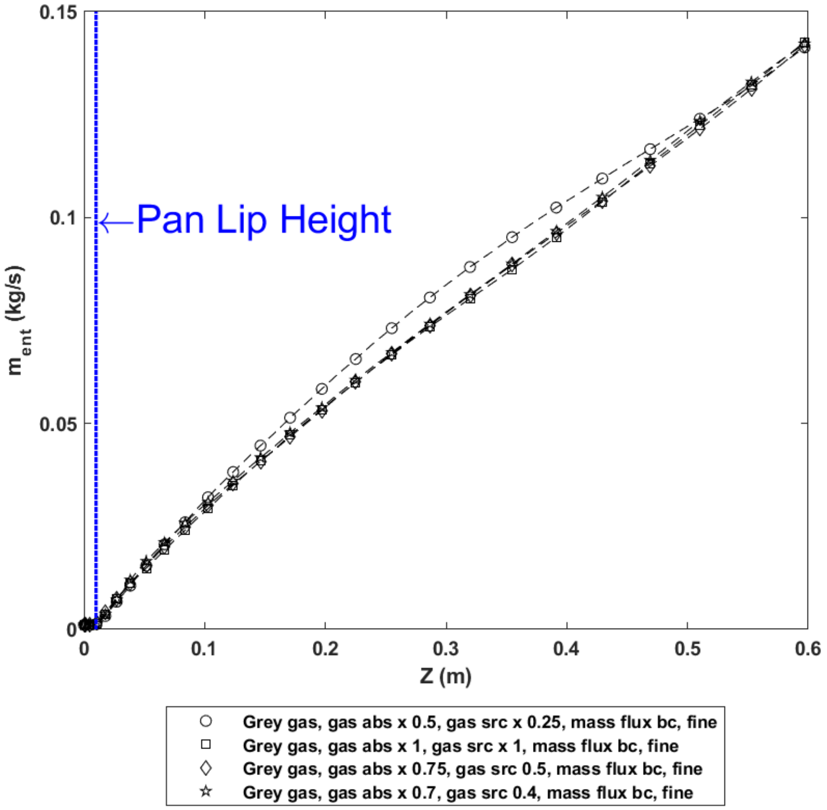

Figure 4-13. Entrainment rate computed as vertical mass flow rate in plume

Modifying the gas absorption coefficient and gas radiation source did not affect the entrainment rate significantly. The percent difference between the SFPE Handbook prediction and the "best" simulation case (prefactors of 0.75, 0.5) was 31.2%, on average from the pool surface to the mean flame height. Extremely high values of percent difference due to low entrainment rate magnitude, near the pool surface, were removed. The difference generally decreased with height as entrainment rate values increased until reaching a value of 21.1% at the mean flame height. For the case with prefactors of (0.5, 0.25), the average percent difference between the threshold data and the SFPE Handbook prediction was 35.9%, while the percent difference at the mean flame height was 23.1%. These comparisons show that the computed entrainment rate agreed well with the engineering correlation, even in the case with the largest deviations from the correlation, as long as the threshold filter was used. In contrast, excluding the threshold in the "best" case yielded values of 92.7% on average and 44.3% at the mean flame height. It is possible that the SFPE Handbook correlations fit data better from experiments and/or simulations in which the burner is flush with the floor. In that case, the threshold filter may act to reduce the entrainment rates computed in this study to rates more comparable with such a setup.

4.1.4. Conclusions from Integrated Buoyancy Flux and Entrainment Rate Analysis

The effect of radiation model calibration upon buoyancy was apparent in the integrated buoyancy flux. Higher absorption coefficient and radiative source term causes higher predicted radiative losses, lower plume temperatures, and lower buoyancy flux. The effect on entrainment rate was less noticeable. Improved agreement in computed entrainment rate with an established engineering correlation was obtained by incorporating a threshold filter which used the mixture fraction value to limit the integration radius to the plume radius. This was also believed to make the values near the pan lip more realistic by excluding contributions from outside of the plume.

4.1.5. Coarse/Fine Comparison

In order to examine the effect of mesh resolution on the simulation results, methanol simulations were performed using a coarse mesh and a fine mesh. Figure 4-14 shows the number of nodes and elements in both meshes and the region in which the mesh was refined to obtain the fine mesh. In the sections that follow, results obtained using both meshes are shown for the cases which produced the radiant fraction in best agreement with experimental data (prefactors of 0.75, 0.5), and which used the mass flux boundary condition. These cases correspond to rows 5 and 6 in Table 4-1.

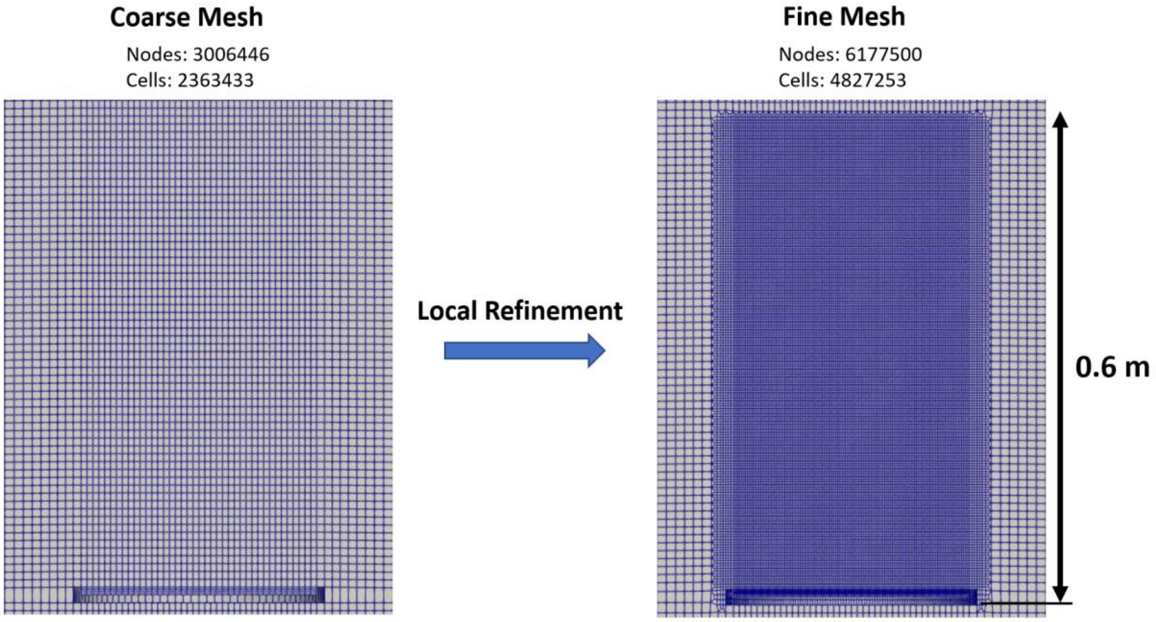

Figure 4-14. Coarse & fine mesh information

4.1.5.1. Centerline Plots

Refining the mesh caused the peak temperature along the centerline to decrease by roughly 50 K and shift to a lower z-value (Figure 4-15a). This location for the peak temperature more closely matches that given by Weckman, but the magnitude is further from the experimental values. The under-prediction of temperature at low heights is mentioned by Hubbard et al. in more detail [3]. The mixture fraction is shown in Figure 4-15b. Because the mixture fraction is lower for the fine mesh above approximately 0.2 m, there appears to be more complete combustion by this height, possibly resulting from better mixing simulated on the finer mesh.

Figure 4-15b and c show that the pressure (gauge) and axial velocity are generally somewhat higher for the fine mesh. Figure 4-15d shows Weckman experimental data as well, which appears to more closely agree with the results from the fine mesh.

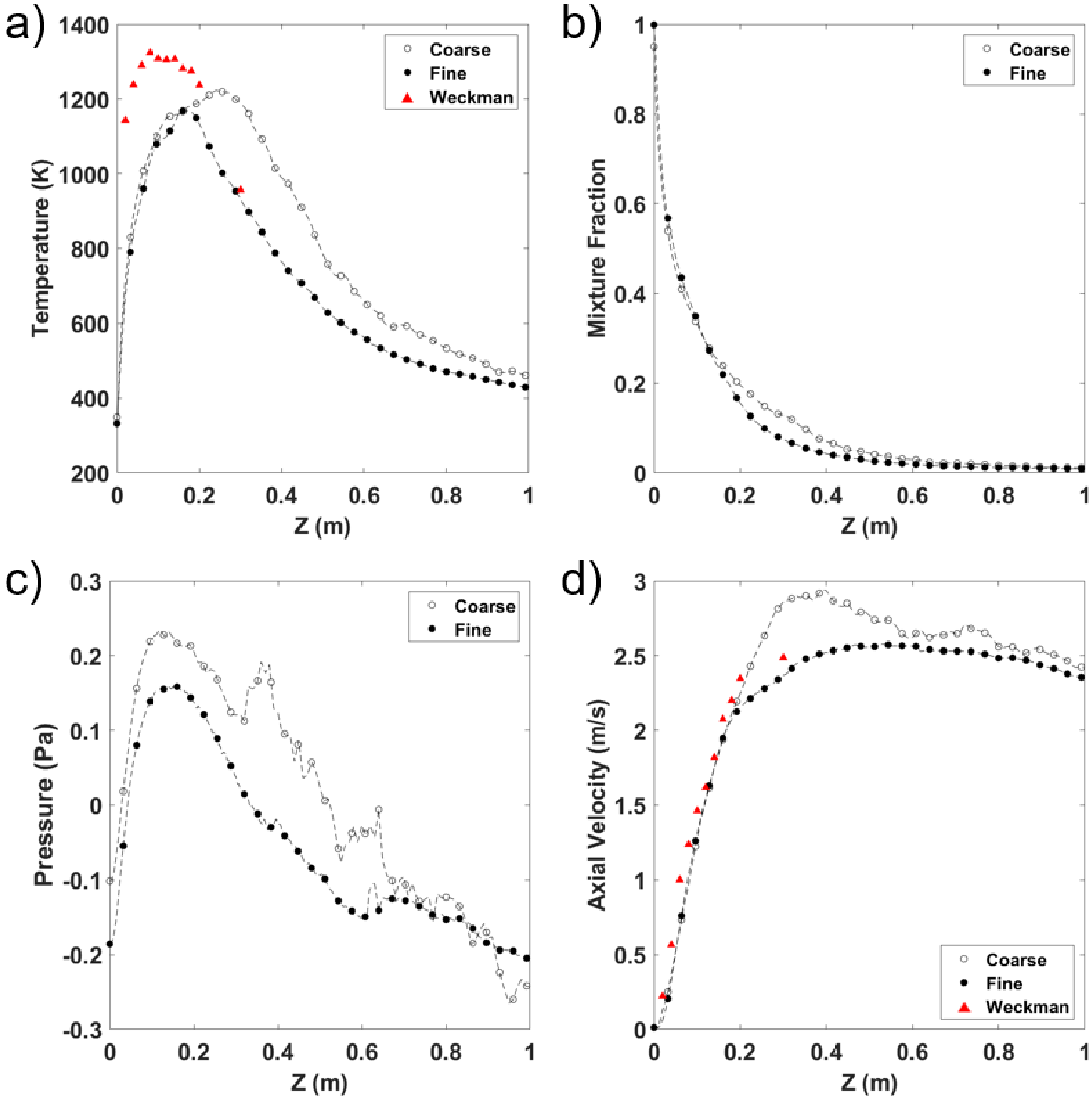

Figure 4-15. a) Temperature, coarse & fine data with experimental values for comparison. b) Mixture fraction. c) Pressure. d) Axial velocity, coarse & fine data with experimental values for comparison. All values are centerline values.

The reported output variable "turbulent kinetic energy (TKE)" from the Fuego simulations was found to be the subgrid TKE, and was significantly affected by mesh resolution. This is due to the LES turbulent closure model used (K-sgs), in which the dissipation of TKE (D_k^{sgs}) in the transport equation for subgrid TKE depends on the cell volume as shown in Eqns. (4.1) and (4.2). The average density is $\bar{\rho}$ in these equations, k^{sgs} is the subgrid TKE, Δ is the grid filter length, and V is the grid cell volume. When the grid cell volume decreases, the grid filter length decreases, which causes the dissipation to increase and the overall source term for production and dissipation to decrease, leading to a lower calculated subgrid TKE. Figure 20 shows that just after the refined region in the fine mesh, the subgrid TKE jumps to higher values before approaching the coarse mesh results.

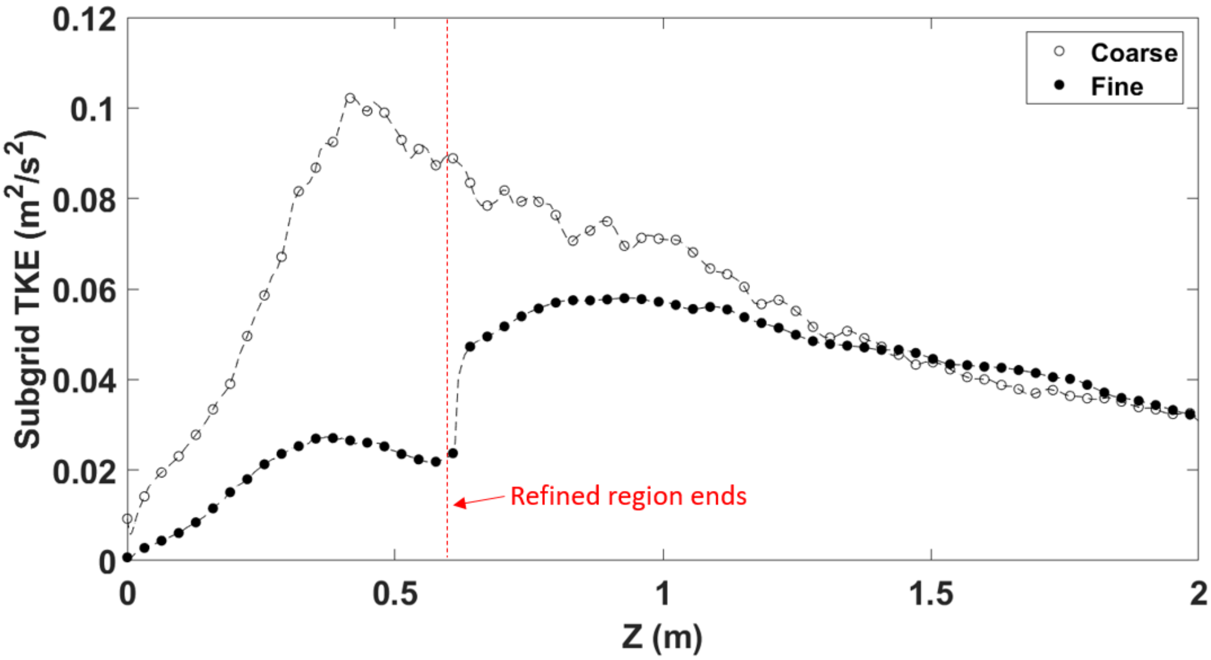

Figure 4-16. Centerline subgrid TKE, coarse/fine comparison

$$D_k^{sgs} = C_\varepsilon \bar{\rho} \frac{(k^{sgs})^{3/2}}{\Delta} \tag{4.1}$$

$$\Delta = V^{1/3} \tag{4.2}$$

Though the effect of the mesh refinement on the subgrid TKE was significant, the effect on the total TKE was much less so. The effect of the subgrid TKE on the total TKE for the fine mesh was shown by computing the resolved TKE and the total TKE using Eqn. (4.3) and comparing the results to Weckman experimental data. Figure 4-17 shows that adding the subgrid TKE to the resolved TKE results in a small increase so that a significant relative discrepancy in TKE due to mesh resolution may be considered negligible.

$$Total\,TKE = \frac{1}{2}\left(\overline{(u')^2} + \overline{(v')^2} + \overline{(w')^2}\right) + subgrid\,TKE \tag{4.3}$$

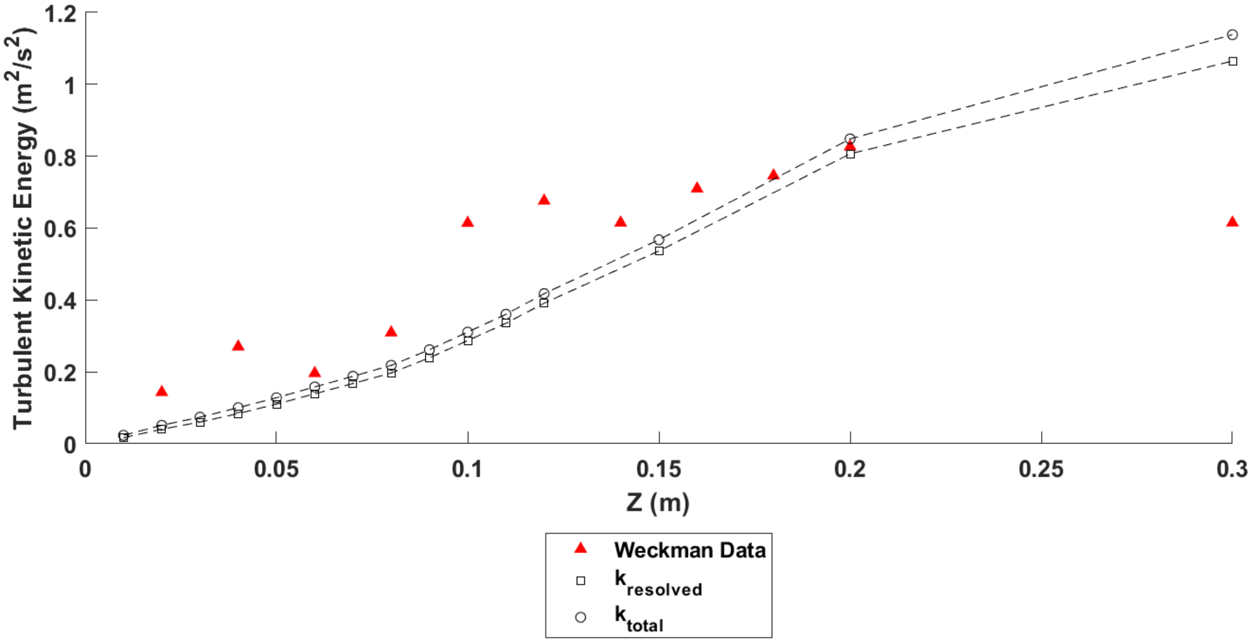

Figure 4-17. Computed total TKE and experimental TKE

4.1.5.2. Integral Quantity Plots

In addition to analyzing several common quantities along the domain centerline to compare results from the coarse and fine meshes, integral quantities were plotted against each other. The radiant fraction (Figure 4-18) is higher for the fine mesh, but by less than 5% at its asymptotic value near $z = 0.6$ m. This indicates that refining the mesh was unnecessary for improvement of the radiant fraction prediction.

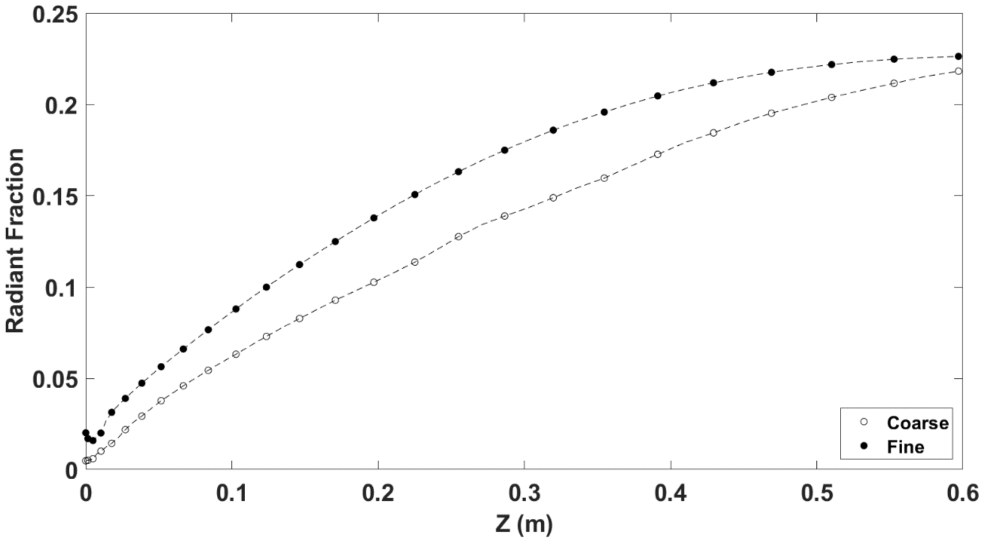

Figure 4-18. Radiant fraction, coarse/fine comparison

The entrainment rate is similar for both meshes, as shown in Figure 4-19. The integrated buoyancy flux, also shown in Figure 4-19, is similar for both meshes at low heights, but is higher for the coarse mesh above $z \approx 0.18$ m. Comparing Figure 4-19 to the plots in the previous section, the coarse mesh resulted in higher temperature, lower density, and higher axial velocity in general, so the higher buoyancy flux is expected.

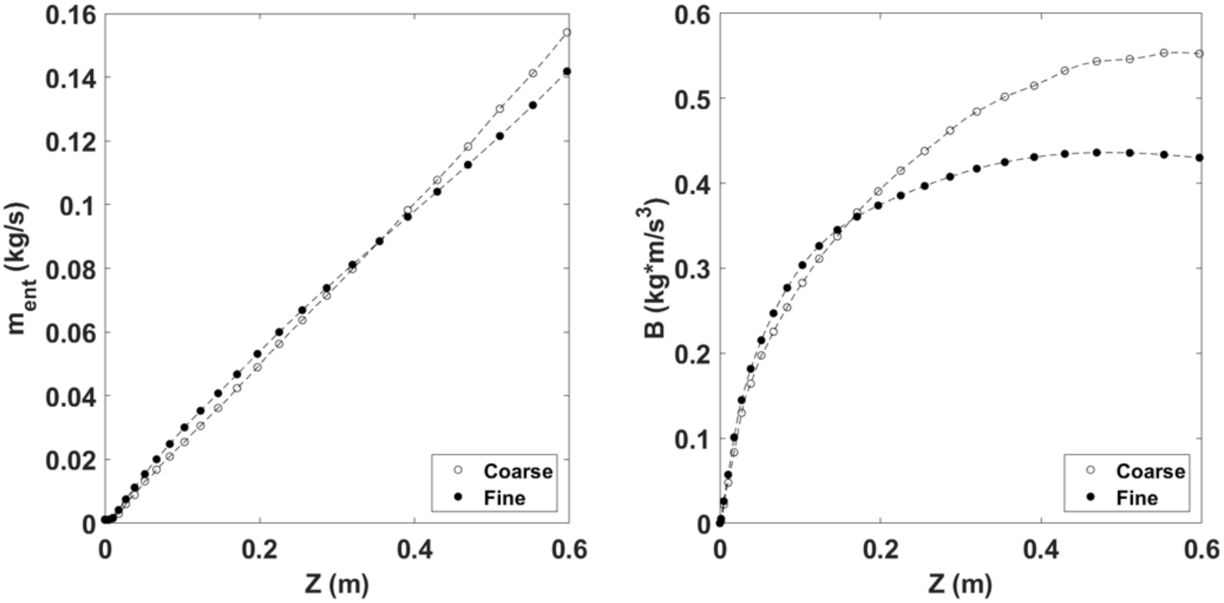

Figure 4-19. Entrainment rate (left) and integrated buoyancy flux (right) for coarse and fine meshes

In Table 4-2, the integrated radiative flux at the pool surface is given for both meshes. Refining the mesh caused a change of approximately 5% in the integrated radiative flux, indicating that mesh refinement was unnecessary for improving the prediction of this quantity. As noted by Hubbard [3], the experimental value is 1.08 kW ± 0.39 kW, so both mesh resolutions yielded results within experimental uncertainty.

Table 4-2. Integrated radiative fluxes for coarse and fine meshes

Mesh	Integrated Radiative Flux (W)	Error = (S-D)/D*100%
Coarse	-810	25.0
Fine	-770	28.7

4.1.6. Conclusions from Coarse/Fine Mesh Comparison

Refining the mesh improved predictions of temperature and axial velocity and had a noticeable effect on several additional quantities. The subgrid turbulent kinetic energy clearly reflected the change in cell size in the refined region, as expected, but the overall TKE was not significantly lower in the finer mesh. Integrated radiative heat flux at the pool surface and radiant fraction values were within 5% difference, and thus mesh refinement was concluded to be unnecessary.

4.1.7. Flame Height

In pool fires, pan diameter is an important parameter. A distinguishing geometric feature of the resulting flame is the flame height. Typically, the flame height is reported as the height to which the visible flame extends. Engineering correlations exist for the estimation of flame height [28]. When flame height is reported from experiments, it is often taken as the height at which the intermittency is 50% [28]. Intermittency is defined as the fraction of time for which a point in space at a certain elevation contains part of the flame. In this study, we analyzed how to define when the flame is "contained" in a computational cell.

In the following sections, both methods are examined, with the primary conclusion from the use of the engineering correlation being that the correct mass flux must be predicted at the pool surface from the simulation in order to accurately predict the flame height. In Section 4.1.7.2, it is shown that multiple parameters may be chosen as threshold variables to calculate intermittency. However, the predicted flame height is sensitive to the parameter used to threshold the data and calculate intermittency.

4.1.7.1. Engineering Correlation

The mean flame height was estimated using the engineering correlation described in Section 2.4.3. In Figure 4-20, the estimated flame height from the engineering correlation is shown for each case, and Table 4-3 gives the identifying information for each case shown in the figure. This correlation gives an accurate prediction of the flame height when the fuel mass flux is either specified or predicted close to the experimentally reported value. However, at lower mass fluxes (Cases 5, 7, and 8), the correlation under-predicts the flame height considerably. Thus, the importance of correctly determining the mass flux at the pool surface is shown if engineering correlations are used.

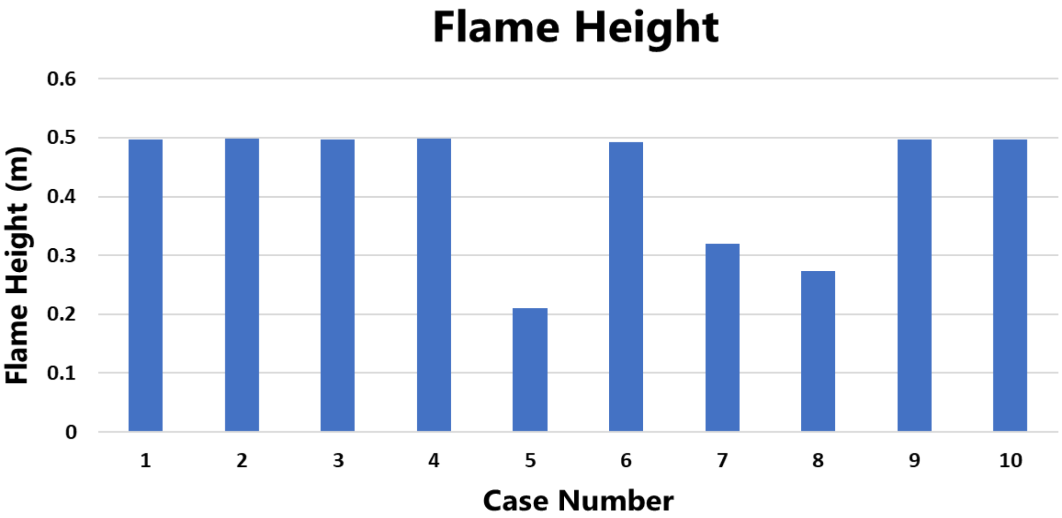

Figure 4-20. Flame height from engineering correlation

Table 4-3. Case identification for flame height plot

Case Number	Boundary Condition	Prefactors
1	Mass flux	0.5, 0.25
2	Mass flux	1,1
3	Mass flux	0.75, 0.5
4	Mass flux	0.7, 0.4
5	Pool	0.5, 0.25
6	Pool	1,1
7	Pool	0.75, 0.5
8	Pool	0.7, 0.4
9	Mass flux*	N/A
10	Pool†	0.7, 0.4
*Spectral radiation model †Uniformly refined mesh		

4.1.7.2. Sensitivity Study Using Intermittency Definition

Flame height from experiments is often calculated using an intermittency definition. Here, the flame height was computed from simulation data using this definition as well. This was done for more direct comparison to experimental data.

Experimentally reported values are often computed using image analysis on a time series of images, or a video of the flame over time. The flame height is based on the height which corresponds to a pixel location at which 50% intermittency occurs. To compute the flame height using simulation data and the intermittency definition, a time-series of data was examined at several heights above and below the experimentally reported flame height. At each of these points, the median temperature (the temperature which is surpassed 50% of the time) at each height was compared to a threshold temperature. The median temperature was used rather than the time-averaged temperature because 1) the median is a better representation of 50% intermittency and 2) the time-average was shown to be biased higher than the median due to large-magnitude fluctuations occurring more frequently above the average than below. When the threshold temperature and median temperature at a given height were in sufficient agreement (5-10%), that height could be taken as the flame height. However, since this method relied on having previous knowledge of the expected flame height, a sensitivity study was done investigating how the predicted flame height varied based on the threshold value chosen for temperature. This analysis was then repeated using the mixture fraction as the threshold variable. Baumgart et al. used the carbon fraction (mixture fraction + soot mass fraction) as a threshold variable for sooting flames [26]. The dataset used for this analysis is the mass flux BC case with prefactors of 0.75, 0.5 (Row 6 in Table 4-1).

A time-series of data was analyzed for each height to determine the minimum timespan which yielded acceptable accuracy. The median temperatures at several heights were computed using five timespans of varying length. Figure 4-21 shows the computed median temperature for these timespans. Figure 4-22 shows the percent difference relative to the 10 second dataset for each of the timespans. The 5 second timespan showed good agreement with the 10 second dataset and was selected as the timespan for analysis.

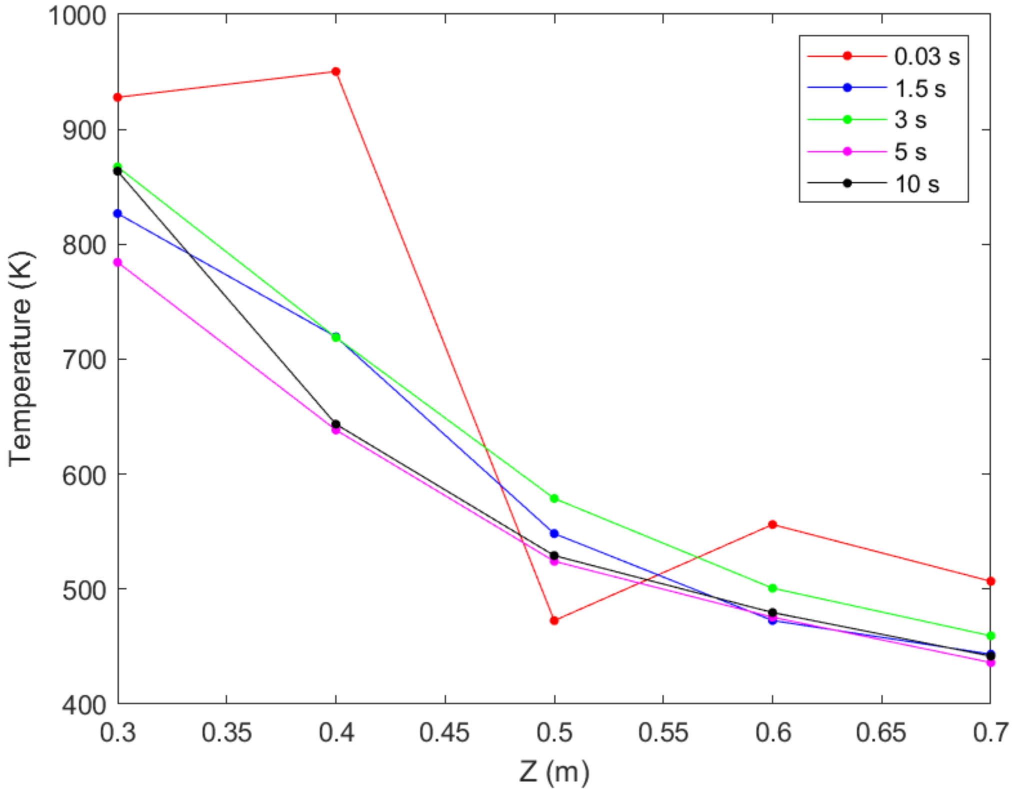

Figure 4-21. Median temperature for multiple time ranges

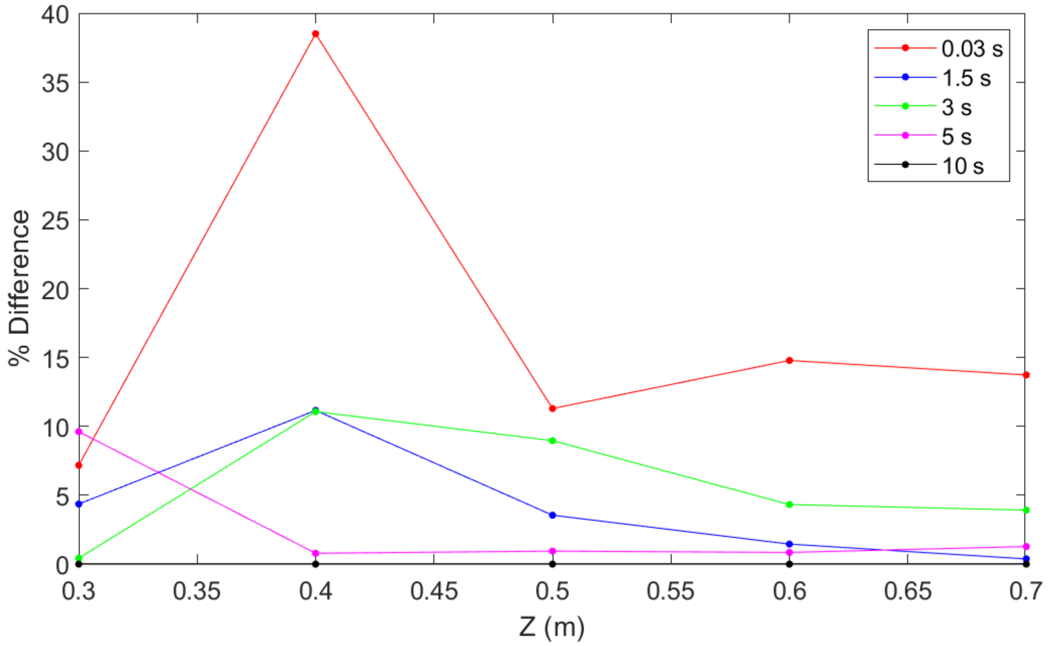

Figure 4-22. Percent differences in median temperature relative to 10 s dataset

In Figure 4-23, the calculated flame height predicted using the intermittency definition is shown for several threshold temperature values. The temperature values were centered around the expected flame height from the engineering correlation as shown in Figure 4-20. This value is slightly below the experimentally expected value but corresponds to the lower mass fluxes seen in the simulation data. The deviation from the expected flame height was significant for both temperature (Figure 27) and mixture fraction (Figure 4-24). The sensitivity of the predicted flame height is summarized below.

- Expected flame height is 0.5 m (see Figure 4-20)
- Mixture fraction at expected flame height: 0.015; Temperature at expected flame height: 524.24 K
- Varying the mixture fraction threshold by +0.005 (28.6%) causes an underprediction of 13.8%
- Varying the mixture fraction threshold by -0.005 (40%) causes an overprediction of 25.5%
- Varying the temperature threshold by +75.76 K (13.5%) causes an underprediction of 13.1%
- Varying the temperature threshold by -74.24 K (15.2%) causes an overprediction of 28.5%
- Variation is higher for lower threshold values of both variables

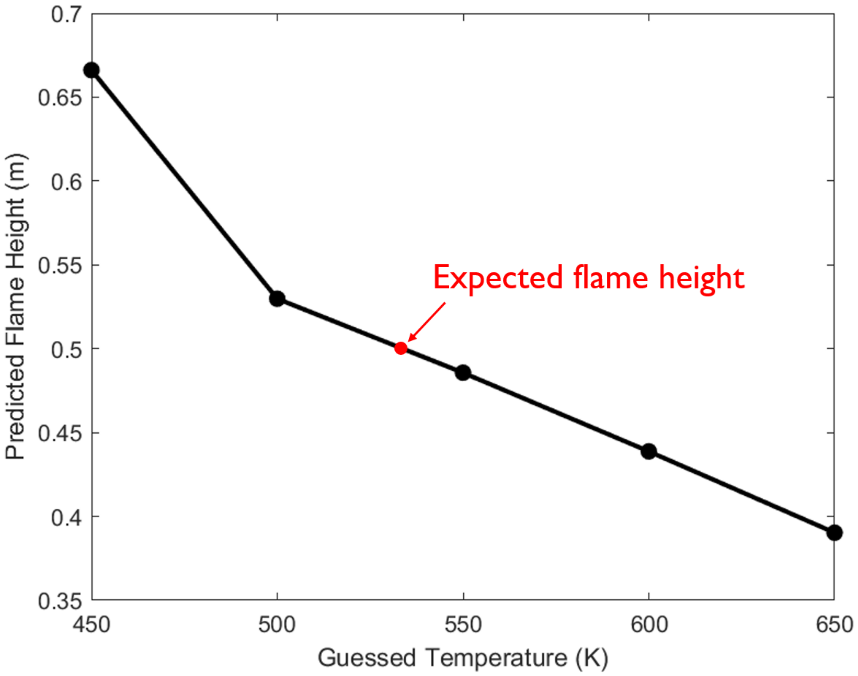

Figure 4-23. Predicted flame height based on temperature threshold

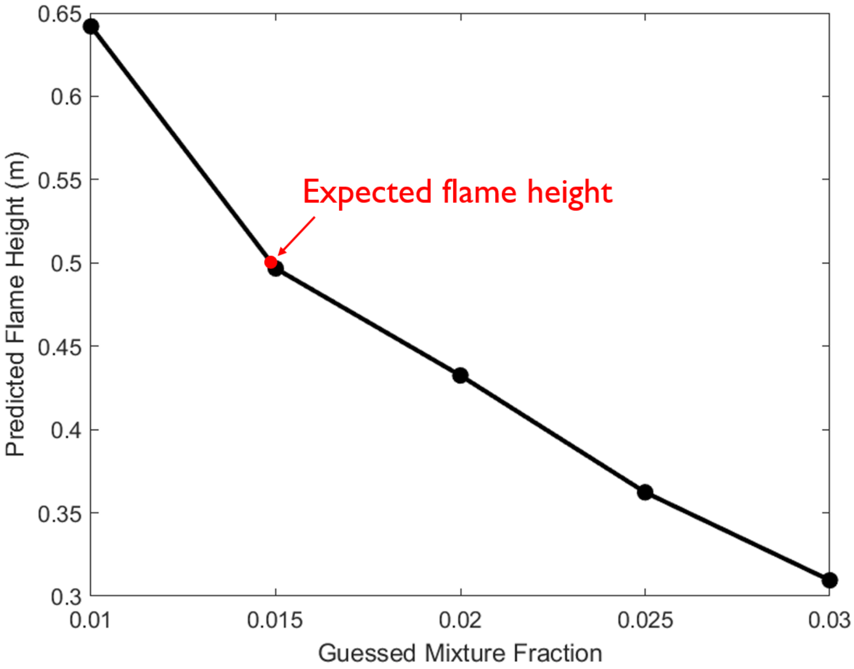

Figure 4-24. Predicted flame height based on mixture fraction threshold

The relative sensitivity of the calculated flame height to the threshold variable chosen was computed on the low and high side of the expected variable. This relative sensitivity was quantified by a ratio defined here as the "Ratio of Percent Differences" (RPD). An example calculation using the mixture fraction as the threshold variable and considering deviations below the expected value is given in Eqn. (4.4). Table 4-4 shows all results. This ratio was found to be higher for deviations on the low side of the expected value, showing greater sensitivity for such deviations. The ratio is also higher for temperature than mixture fraction, indicating less sensitivity in the computed flame height when mixture fraction is used as the threshold variable. This conclusion is only valid when changes to the threshold variable are considered in terms of relative magnitude, since mixture fraction is much lower than temperature.

$$RPD_{L,Mixture\,Fraction} = \frac{25.5\%}{40.0\%} \approx 0.6 \qquad (4.4)$$

Table 4-4. Ratios of percent differences.
Shows relative sensitivity of flame height to threshold variable.

	RPD_H	RPD_L
Mixture Fraction	0.5	0.6
Temperature	1.0	1.9

4.1.7.3. Conclusions from Flame Height Analysis

Flame height was computed using a common engineering correlation. The results showed good agreement with experimental data when the correct fuel mass flux at the pool surface was predicted or prescribed. An intermittency definition of flame height was also used to compute the mean flame height. Both temperature and mixture fraction were used as threshold variables to define intermittency. Flame height computed from the intermittency definition showed significant sensitivity to the value of the threshold variable. The sensitivity was shown to be lower for the mixture fraction and when the threshold value is guessed higher, instead of lower, than the true median value.

4.2. Heptane

The second type of fuel analyzed in this report was heptane, chosen because it is a sooting fuel and provides another good validation case. A 0.3-m diameter heptane pool fire was modeled and simulated using SIERRA/Fuego & Nalu, with the same modeling scheme as was used for methanol, but with the inclusion of a soot model. The presence of soot was expected to significantly affect radiative heat transfer, but not dominate it as in more heavily-sooting fires. Choi et al. [35] stated that for a 10-cm diameter heptane pool fire, 60% of the radiative heat feedback to the pool surface was due to soot. This is lower than the approximately 90% due to soot for a similarly-sized toluene fire [36, 37]. Soot evolution was taken into account in the flamelet library used in this study and the resulting soot mass fraction, soot absorption coefficient, and soot radiative source term modified the inputs to the radiation model. The flamelet library was developed for use with heptane, and had a heptane boiling point boundary condition (temperature = 371.6 K). The gray-gas model parameters ($\mu_{a,g}, e_g$) were not modified (i.e. equivalent prefactors were (1, 1)) as in the methanol simulations due to the assumption that soot components would be dominant.

In Section 4.2.1, the quantities which exist in the radiation model for both sooting and non-sooting fires are shown for heptane and methanol. Thus, the effect of the fuel type and of the presence of soot can be seen. The methanol case used for comparison has prefactors of (0.75, 0.5) shown in Row 6 of Table 4-1. Both the heptane and methanol simulations used 0.3-m diameter pans, with the pool surface elevated from the floor by 0.25 m. The fuel mass flux was prescribed as 0.015 kg/m^2-s at the surface.

Additional quantities describing the fire physics and soot evolution were computed for the heptane fire, and are shown in Section 4.2.2. The geometry used in the simulations described in the following sections is identical to that of the methanol simulations of Section 4.1. Heptane simulations were performed on the coarse mesh only. Quantities which were also computed for methanol are plotted for both fuels for comparison. It should be noted that the methanol results are from simulations on the fine mesh.

4.2.1. Radiation Model Analysis

The soot number of moles per mass, or number per mass mixture (N) is shown along with the soot mass fraction (M) in Figure 4-25. The effect of oxidation is seen in the soot mass fraction by the drop after the maximum at $z \approx 0.4$ m, where physically, oxidation consumes the soot particles more strongly. The soot mass fraction appears to be significantly lower than the experimentally expected value, which is O(10^{-3}) [21, 35].

The soot model used is that developed by Aksit and Moss [33], which uses acetylene as the precursor. Soot formation mechanisms may need to be adjusted for heptane in the current model given the difference between simulation and experimental soot mass fraction.

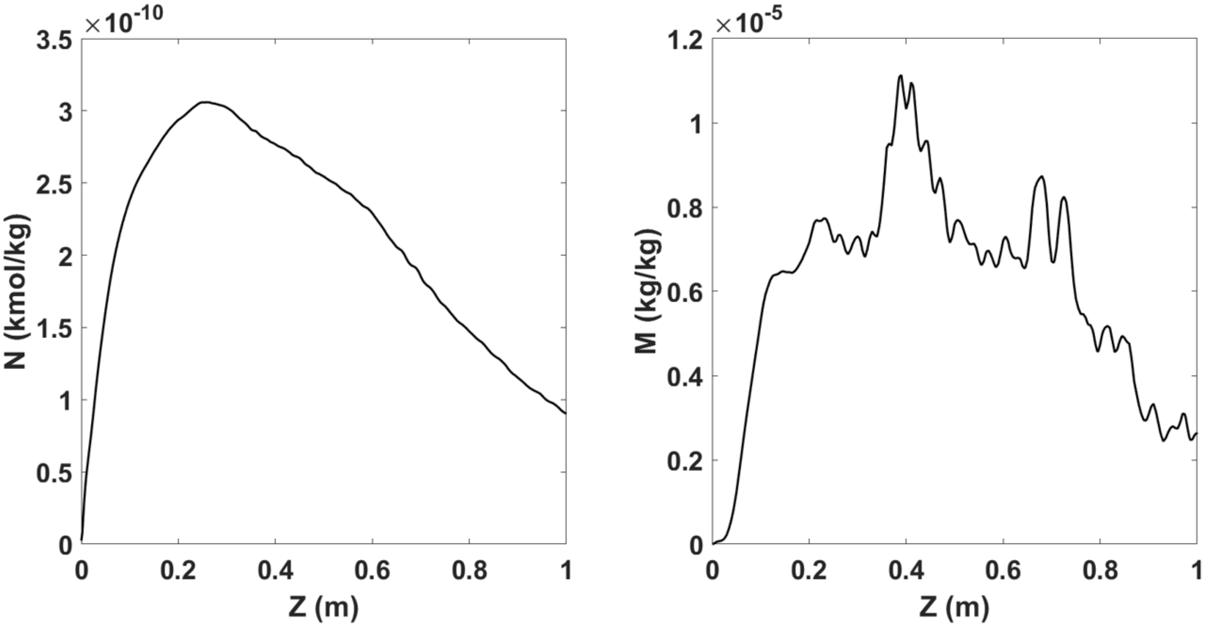

Figure 4-25. Soot number per mass mixture (N) and soot mass fraction (M) for heptane. Values are along centerline.

In Figure 4-26a, the absorption coefficient is shown for heptane and methanol. The absorption coefficient is greater for heptane for all heights shown, but the effect of soot on the absorption coefficient is very small. Heptane is not a heavily-sooting fuel [35], and thus, soot is not expected to dominate radiative heat transfer in heptane flames. However, the effect of soot is likely underpredicted in this study based on the soot mass fraction. Because the radiant fraction is still near experimentally reported values, the effect of the gas phase on radiative heat transfer may be overpredicted and the soot contribution under-predicted. The two may offset each other. This may be partially due to the use of the initial steady state fuel mass flux boundary condition rather than the bulk boiling period boundary condition. A similar statement may be made for the radiative source term (Figure 4-26b). The radiative intensity is higher for heptane as a result of the higher radiative source term, and this is reflected in a higher radiative flux (Figure 4-26c) and scalar flux (Figure 4-26d). However, the radiative flux is higher over a region (approximately $0.18 \leq z \leq 0.35$) for methanol.

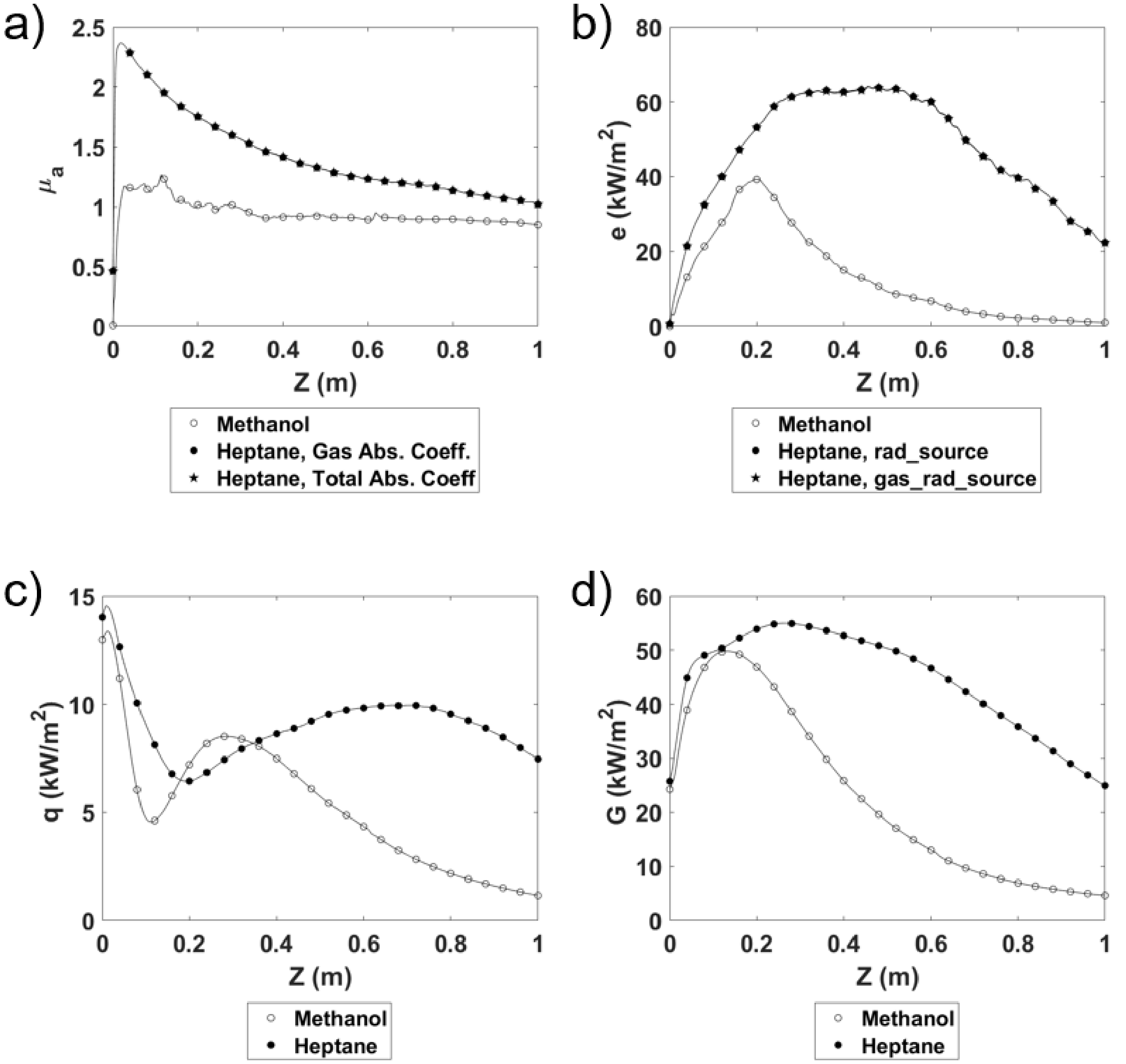

Figure 4-26. Time-averaged, centerline plots of radiation model quantities. a) Absorption coefficient for methanol and heptane. b) Radiative source term for Boltzmann Radiative Transport Equation. c) Vector magnitude of radiative flux. d) Scalar flux.

Below about 0.3 m, the enthalpy sink term is higher for the methanol data (Figure 4-27), but the effect of the absorption coefficient is to make the dq/dx term higher for heptane for all heights. Because the radiative sink term in the enthalpy equation is higher for heptane, the enthalpy deficit is expected to be greater for heptane. This greater enthalpy deficit reflects larger radiative losses.

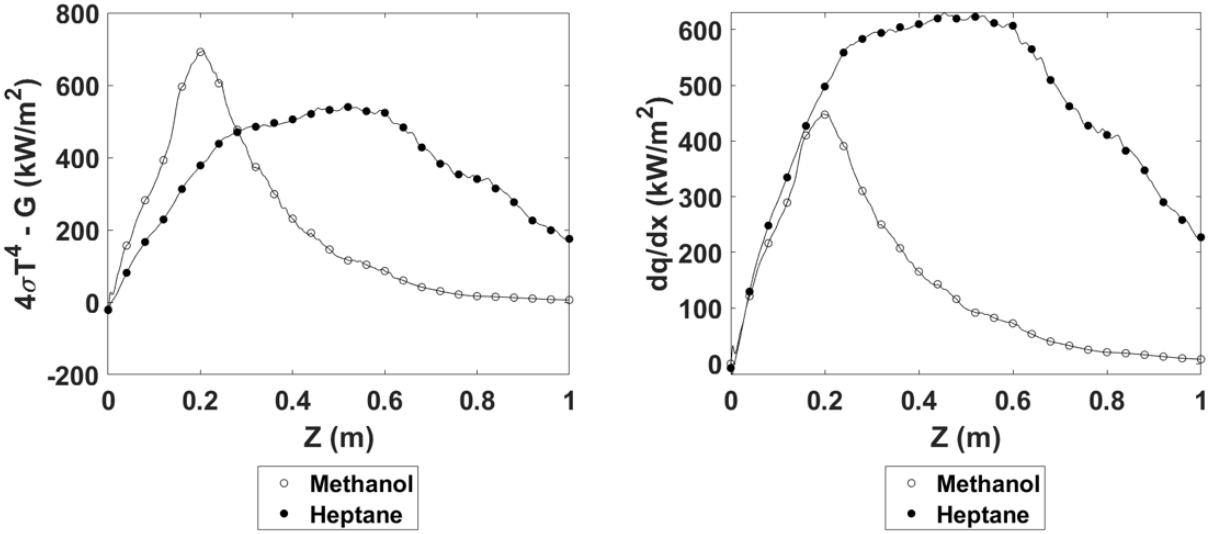

Figure 4-27. Difference of terms in enthalpy sink (left), and radiative sink term for enthalpy transport equation (right). Values are along centerline.

Figure 4-28 shows that the integrated enthalpy deficit flux is significantly larger for heptane, as expected from the larger enthalpy sink term. The integrated mixture fraction flux is similar for both fuels.

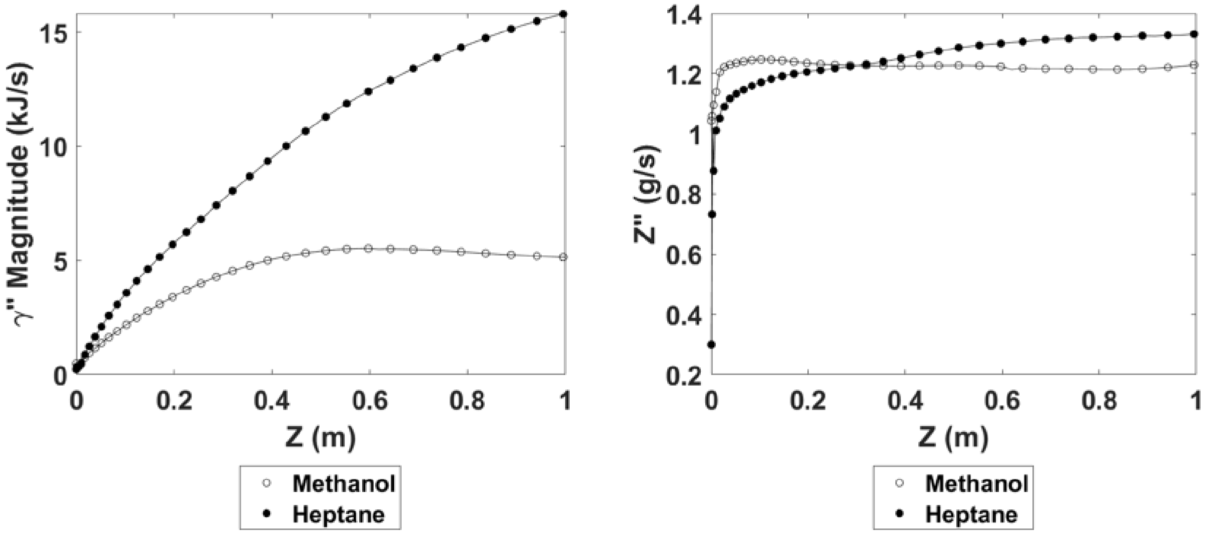

Figure 4-28. Integrated enthalpy deficit flux (left), and integrated mixture fraction flux (right). Values are integral values at each height.

Despite the integrated enthalpy deficit flux being significantly larger for heptane, the radiant fraction is comparable for the two fuels. This is largely due to the higher heat of combustion of heptane (44.4 MJ/kg vs 19.9 MJ/kg). The radiant fraction is higher for methanol below $z \approx 0.65$ m, indicating that radiative losses play a larger relative role in the heat loss of the methanol fire at these heights. This result is surprising due to the presence of soot in heptane and its absence in methanol. However, because the soot contributions to radiative losses in the heptane simulations were underpredicted, this phenomenon may not be real.

Experimental data for a heptane fire with a similar fuel mass flux gives the radiant fraction as approximately 0.25 [16], vs. the methanol value of 0.22. These values correspond to a height of $z \approx 0.8$ m in Figure 4-29.

It should be noted that the fuel mass flux used as a boundary condition in the heptane simulations was the same as that used in the methanol simulations (0.015 kg/m^2-s), and corresponds to an initial steady state condition for such a heptane fire rather than a bulk boiling condition.

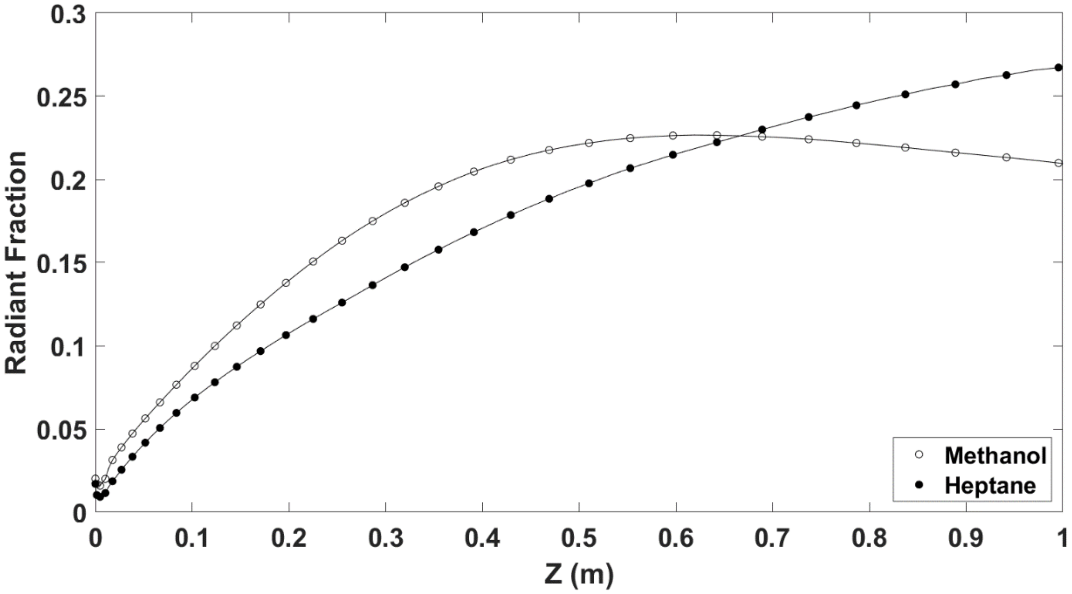

Figure 4-29. Radiant fraction, methanol/heptane comparison. Values are integral values at each height.

4.2.2. Integral Quantities

Several quantities were identified as quantities of interest for heptane, including the radiative source term for the BRTE, radiative heat flux, soot mass fraction, integrated enthalpy deficit flux, and radiant fraction shown in the previous section.

Additional quantities of interest not directly included in the radiation model analysis include the entrainment rate, integrated buoyancy flux, and soot fraction, and these quantities are shown below.

Figure 4-30 shows that the centerline temperature for both fuels is similar or higher for methanol below $z \approx 0.2$ m, and is then much higher for heptane. This contributes to a significantly higher integrated buoyancy flux above this height for heptane.

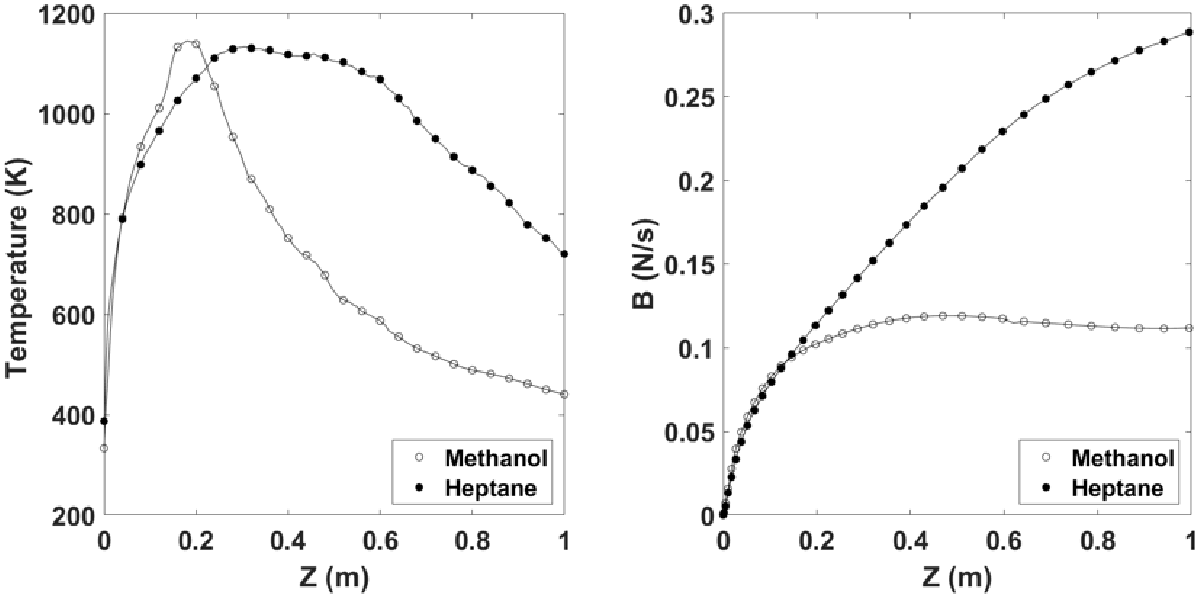

Figure 4-30. Centerline temperature (left) and integrated buoyancy flux (right)

The entrainment rate is defined and explained in Section 2.4.1 and is shown in Figure 4-31. This quantity is similar for the two fuels up to $z \approx 0.3$ m and higher for heptane afterward. Generally increased temperature in the heptane plume causes generally higher buoyant acceleration, which drives the entrainment of more air into the plume. However, the temperatures are lower in the heptane plume below $z \approx 0.2$ m , and this is reflected in the integrated buoyancy flux and in the entrainment rate.

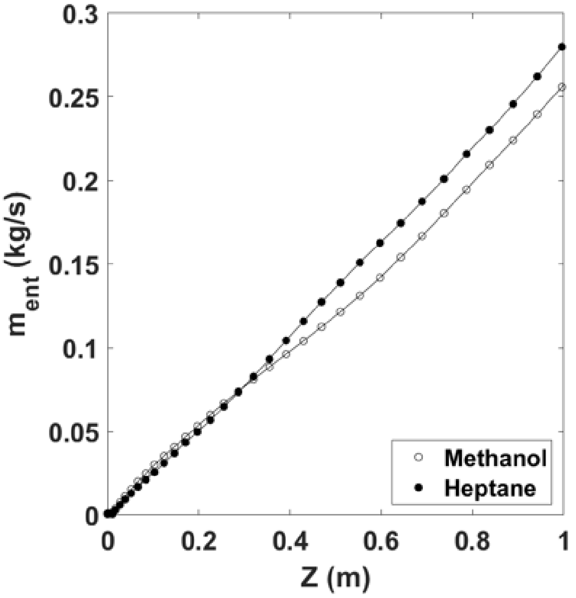

Figure 4-31. Entrainment rate

Integrated soot mass flux is defined in Equation (4.5) and shown in Figure 4-32. The soot mass flux is a cross-flame area integral of the soot advection terms and describes the vertical mass flow rate of soot in the flame. It follows a similar trend to the soot fraction, defined in Equation (4.6) and shown in Figure 4-32. The soot fraction is an integral measure of the soot content in the flame and describes the ratio of the soot mass flux to fuel mass flux in the flame [26].

$$Y_s'' = \int_0^\infty \rho u Y_s r dr \tag{4.5}$$

$$x_s = \frac{Y_s''}{Z''} = \frac{\int_0^\infty \rho u Y_s r dr}{\int_0^\infty \rho u Z r dr} \tag{4.6}$$

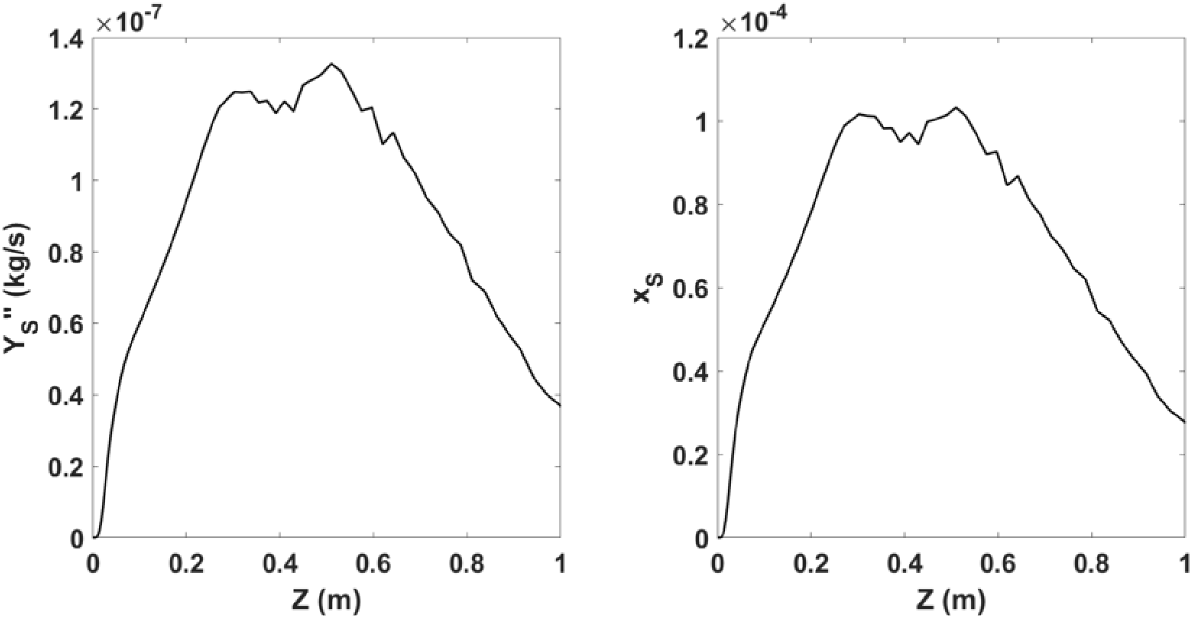

Figure 4-32. Integrated soot mass flux (left) and soot fraction (right)

In Table 4-5, the integrated radiative flux at the pool surface is shown for both fuels. The radiative flux to the surface is higher for heptane, as expected from the higher radiant fraction and other radiation model parameters examined above. An integral of the data in [10] using the trapezoidal rule yields a value of around 1.1 kW. The fuel mass flow rate in this experiment was significantly higher than that of the simulation, and the uncertainty in the measurements is likely high (see Section 4.2.1) [10]. Thus, the simulation result is thought to show sufficient agreement. However, it may be possible that gas radiation is over-predicted, and soot radiation is under-predicted. The level to which each contribution may be inaccurate needs additional study.

Table 4-5. Integrated radiative flux for methanol and heptane

Mesh	Integrated Radiative Flux (W)
Methanol	-770
Heptane	-875

4.2.3. Conclusions from Heptane Analysis

A flamelet library was developed for use in the modeling of a 0.3-m diameter heptane pool fire using SIERRA/Fuego and Nalu. Both the heptane and methanol simulations used the same prescribed mass flux boundary condition, which corresponded to an initial steady state for heptane rather than the bulk boiling condition. The contributions of soot to radiative heat transfer were not expected to be dominant for heptane since it is not a heavily-sooting fuel. Soot mass fractions, for single points in space, were several orders of magnitude lower than experimental data. More work is needed to understand if experimental values represent more of a volume average than a temporally averaged point measurement. Soot contributions to the absorption coefficient and radiative source term were insignificant, compared to gas contributions, which may be due to the underprediction of soot content in the flame. However, the radiant fraction resulting from the simulations agreed with experimentally reported values within about 10%. It is possible that gas contributions were over-predicted and soot contributions were under-predicted, and that the two effects offset each other to some degree. More work is needed to quantify the relative contributions of gas and soot radiation in heptane fires.

5. CONCLUSIONS

Medium-scale hydrocarbon pool fires were simulated using Sandia National Laboratories' SIERRA/Fuego low-Mach number reacting flow code for validation purposes. Fuels simulated included methanol (non-sooting) and heptane (sooting). The radiation model in the coupled Fuego/Nalu simulations was analyzed in depth and the dependence of model outputs on model inputs was examined. Additional quantities describing plume physics were computed and analyzed.

A detailed analysis of the radiation model was performed which gave insight into the relationship between radiation model quantities and the effect of the absorption coefficient and radiative source terms on other quantities. The resulting mechanistic understanding of the model improved the quality and detail of feedback to the simulating engineer regarding the effects of model parameters. Radiative intensity, scalar flux, and the radiative enthalpy sink term increased with increasing absorption and radiative source term magnitude. Consequently, radiant fraction increased.

The radiation model used a gray-gas assumption and overpredicted the radiant fraction with default parameters. Successful calibration of the model was achieved by modifying gray-gas model parameters such that the experimentally reported radiant fraction was predicted.

The effect of radiative losses on buoyancy was illustrated by the integrated buoyancy flux. This quantity decreased with increased radiative losses. Entrainment in the plume was quantified by the mass entrainment rate. A threshold limiting the integration radius improved agreement of this quantity with an engineering correlation given in the SFPE Handbook of Fire Protection Engineering [28].

Methanol simulations included multiple boundary condition types and two levels of mesh refinement. The finer mesh resulted in improved predictions of most quantities, but did not significantly improve predictions of radiative heat flux or radiant fraction.

Flame height was computed using an engineering correlation and the correct prediction or specification of fuel mass flux was shown to be important for accurate predictions of flame height with this correlation. Flame height was also calculated using an intermittency definition. A sensitivity study describing the sensitivity of computed flame height to the value of the threshold variable was performed.

The radiation model was examined for heptane using results from a heptane flamelet library. Corresponding cases of methanol and heptane simulation data were compared to examine the effect of soot and of increased gas phase radiation properties on the radiative heat transfer in the flame. Soot levels were thought to be significantly underpredicted, indicating potential for further development of soot formation mechanisms in the model used. Gas phase contributions to radiative heat transfer were likely overpredicted.

REFERENCES

1. Domino, S., Moen, C., Burns, S., Evans, G. . *SIERRA/Fuego: A Multi-Mechanics Fire Environment Simulation Tool*. in *41st Aerospace Sciences Meeting and Exhibit*. 2003. Reno, Nevada.
2. *Verification & Validation*. [cited 2021 Sept.]; Available from: https://www.sandia.gov/asc/advanced-simulation-and-computing/verification-validation/.
3. Hubbard, J.A., Hansen, Michael A., Kirsch, Jared R., Hewson, John C., Domino, Stefan P., *Medium Scale Methanol Pool Fire Model Performance Validation*. 2021.
4. Weckman, E.J. and A.B. Strong, *Experimental Investigation of the Turbulence Structure of Medium-Scale Methanol Pool Fires*. Combustion and Flame, 1996.
5. Buch, R., Hamins, A., Konishi, K., Mattingly, D., and Kashiwagi, T., *Radiative Emission Fraction of Pool Fires Burning Silicone Fluids*. Combustion and Flame, 1997.
6. Falkenstein-Smith, R., K. Sung, J. Chen, and A. Hamins, *Chemical Structure of Medium-Scale Liquid Pool Fires*. Fire Safety Journal, 2020.
7. Falkesntein-Smith, R., K. Sung, Chen, J., Harris, K., A. Hamins, *The Structure of Medium-Scale Pool Fires*. 2020, National Institute of Standards and Technology: Gaithersburg, MD.
8. Hamins, A., Lock, A., *The Structure of a Moderate-Scale Methanol Pool Fire*. 2016, National Institute of Standards and Technology: Gaithersburg, MD.
9. Kim, S.C., K.Y. Lee, and A. Hamins, *Energy Balance in Medium-Scale Methanol, Ethanol, and Acetone Pool Fires*. Fire Safety Journal, 2019.
10. Klassen, M., Gore, J. P., *Structure and Radiation Properties of Pool Fires*. 1994, National Institute of Standards and Technology: Gaithersburg, MD.
11. Wang, Z., Tam, W.C, Chen, J., Lee, K.Y., and Hamins, A., *Thin Filament Pyrometry Field Measurements in a Medium-Scale Pool Fire*. Fire Technology, 2019.
12. Klassen, M., Gore, J. P., *Structure and Radiation Properties of Pool Fires*. 1992, Purdue University: Thermal Sciences and Propulsion Center, School of Mechanical Engineering.
13. Ma, L., Nmira, F., Consalvi, J. , *Large Eddy Simulation of medium-scale methanol pool fires - effects of pool boundary conditions*. Combustion and Flame, 2020.
14. Orloff, L., De Ris, J. *Froude Modeling of Pool Fires*. in *Nineteenth Symposium (International) on Combustion*. 1982. The Combustion Institute.
15. Ahmed, M., Trouve, A., *Large eddy simulation of the unstable flame structure and gas-to-liquid thermal feedback in a medium-scale methanol pool fire*. Combustion and Flame, 2021.
16. Vinay C. Raj, Prabhu, S., *Measurement of geometric and radiative properties of heptane pool fires*. Fire Safety Journal, 2018.
17. Hamins, A., M. Klassen, J. Gore, S. Fischer, T. Kashiwagi, *Estimate of Flame Radiance via a Single Location Measurement in Liquid Pool Fires*. Combustion and Flame, 1991.
18. Koseki, H. Hayasaka, H., *Estimation of Thermal Balance in Heptane Pool Fire*. Journal of Fire Sciences, 1989.
19. Kang, Q., Lu, S., Chen, B., *Experimental study on burning rate of small scale heptane pool fires*. Chinese Science Bulletin, 2010.
20. Chen, B., Lu, S., Li, C., Kang, Q., Yuan, M., *Unsteady burning of thin-layer pool fires*. Journal of Fire Sciences, 2011.
21. Kamiuto, K., Itoh, R., Higashi, K., Yano, H., *Characterization of Carbon Particulates in Diffusion Flames*. JSME Internation Journal, 1996.
22. Kang, Y., Wen, J., *Large Eddy Simulation of a Small Pool Fire*. Combustion Science and Technology, 2004.

23. Chatterjee, P., Wang, Y., Meredith, K., Dorofeev, S., *Application of a subgrid soot-radiation model in the numerical simulation of a heptane pool fire.* Proceedings of the Combustion Institute, 2015.
24. Wu, B., Roy, S., Zhao, X., *Detailed modeling of a small-scale turbulent pool fire.* Combustion and Flame, 2020.
25. Colin Aro, A.B., Alex Brown, Shawn Burns, et al., *SIERRA Low Mach Module: Fuego Theory Manual - Version 5.0*, S.N. Laboratories, Editor. 2021. p. 44, 52.
26. Baumgart, A., Voskuilen, T., Sakievich, P., Hewson, J., *Soot and radiation interactions in turbulent jet flames studied with Reynolds-averaged Navier-Stokes simulations*, in *2019 WSSCI Fall Technical Meeting.* 2019: Albuquerque, New Mexico.
27. Koo, H., Hewson, J. C., Knaus, R. C. . *LES Soot-Radiation Predictions of Buoyant Fire Plumes.* in *Western States Section of the Combustion Institute - Spring 2018 Meeting.* 2018. Oregon State University.
28. Heskestad, G., *Fire Plumes, Flame Height, and Air Entrainment*, in *SFPE Handbook of Fire Protection Engineering.* 2016, Springer.
29. Heskestad, G., *Fire Plume Air Entrainment According to Two Competing Assumptions*, in *21st Symposium on Combustion.* 1986, Combustion Institute: Pittsburgh, PA.
30. Cetegen, B.M., Zukoski, E. E., and Kubota, T., *Entrainment and Flame Geometry of Fire Plumes*, in *Daniel and Florence Guggenheim Jet Propulsion Center.* 1982, California Institute of Technology.
31. Delichatsios, M.A., *Air Entrainment into Buoyant Jet Flames and Pool Fires.* Combustion and Flame, 1987(70): p. 33-46.
32. Iqbal, N., Salley, M. H., *Fire Dynamics Tools (FDT): Quantitative Fire Hazard Analysis Methods for the U.S. Nuclear Regulatory Commission Fire Protection Inspection Program*, O.o.N.R.R. U.S. Nuclear Regulatory Commission, Editor. 2004: Washington, DC. p. 3-17.
33. Aksit, I., Moss, J. , *A hybrid scalar model for sooting turbulent flames.* Combustion and Flame, 2006.
34. Ekoto, I.W., Ruggles, A. J., Creitz, L. W., Li, J. X. , *Updated jet flame radiation modeling with buoyancy corrections.* International Journal of Hydrogen Energy, 2014.
35. Choi, M., Hamins, A., Rushmeier, H., Kashiwagi, T. *Simultaneous Optical Measurement of Soot Volume Fraction, Temperature, and CO2 in Heptane Pool Fire.* in *Twenty-Fifth Syposium (International) on Combustion.* 1994.
36. Klassen, M., *Ph.D. Thesis.* 1992, University of Maryland: College Park, MD.
37. Klassen, M., Sivanthanu, Y. R., Gore, J. P., *Simultaneous Emission Absorption Measurements in Toluene-Fueled Pool Flames: Mean and RMS Properties* Combustion and Flame, 1992.
38. Reddy, M., De, A., Yadav, R., *Effect of precursors and radiation on soot formation in turbulent diffusion flame.* Fuel, 2015.
39. Lemaire, R., Faccinetto, A., Therssen, E., Ziskind, M., Focsa, C., Desgroux, P. , *Experimental comparison of soot formation in turbulent flames of Diesel and surrogate Diesel fuels.* Proceedings of the Combustion Institute, 2009.

APPENDIX A. METHANOL INTEGRAL QOI PLOTS – ALL CASES

A.1. Radiant Fraction, Integrated Buoyancy Flux, and Entrainment Rate, All Methanol Simulation Cases

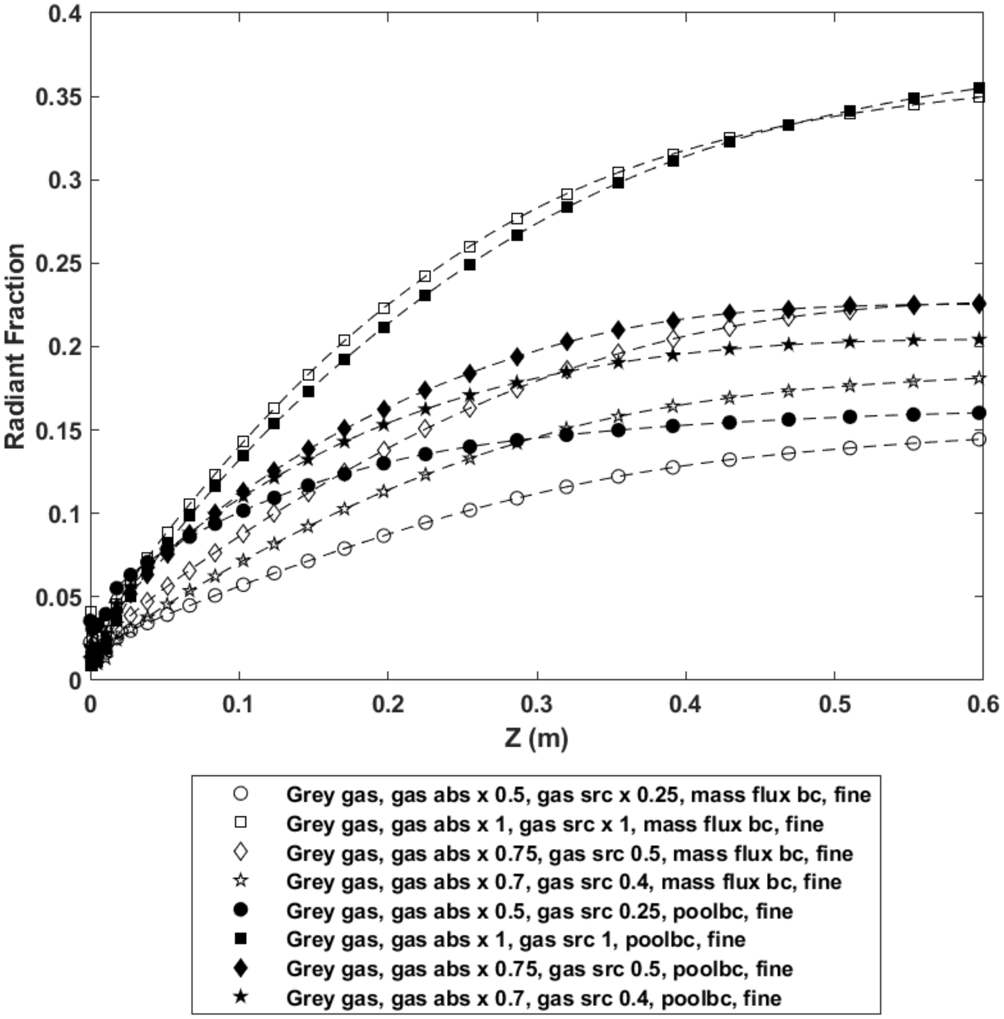

Figure 5-1. Radiant fraction, methanol, both BCs

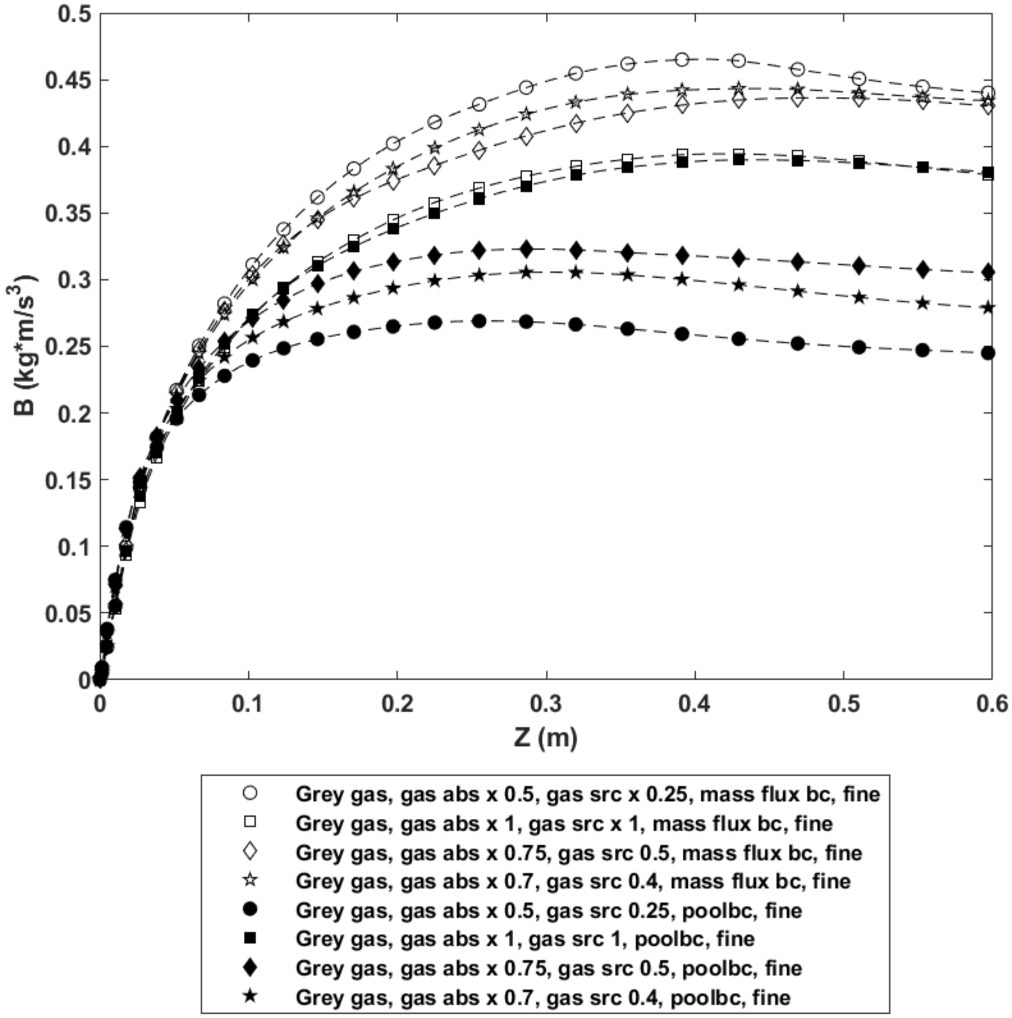

Figure 5-2. Integrated buoyancy flow, methanol, both BCs

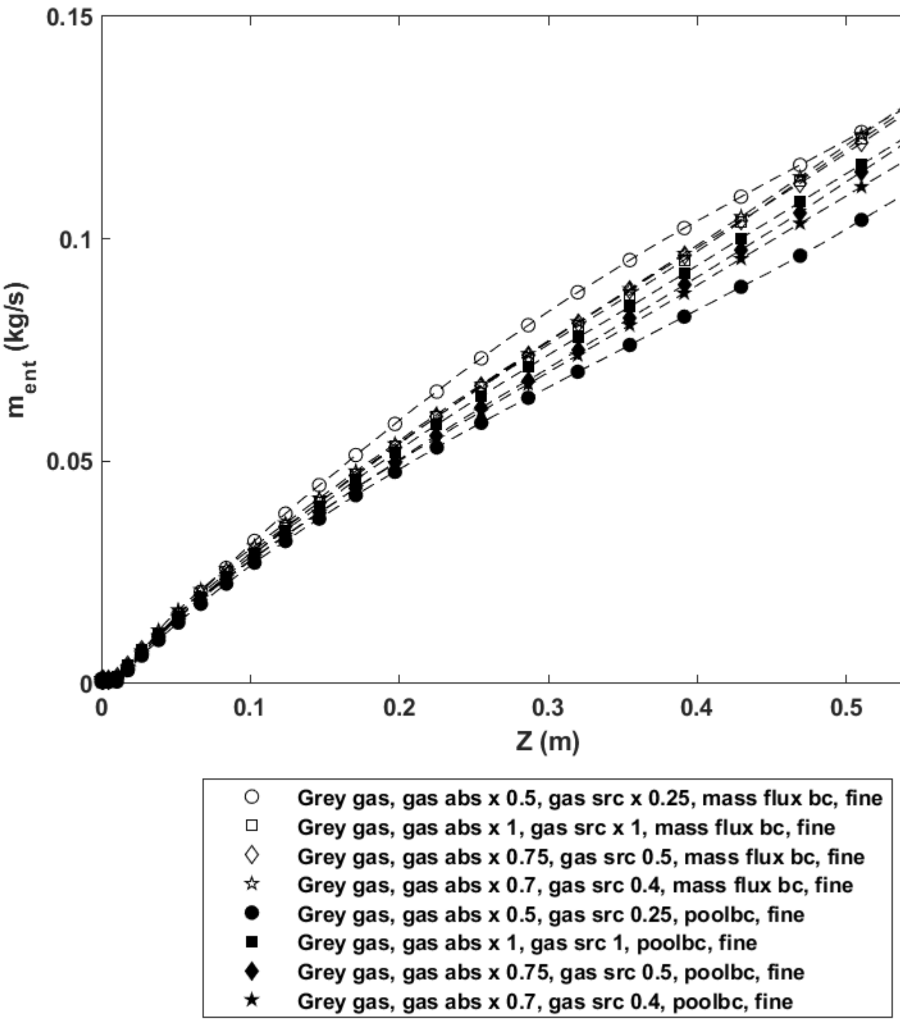

Figure 5-3. Entrainment rate, methanol, both BCs

This page left blank

DISTRIBUTION

Email—Internal

Name	Org.	Sandia Email Address
Lance, Blake	1544	blance@sandia.gov
Armstrong, Elizabeth	1541	earmstr@sandia.gov
Phinney, Leslie	1514	lmphinn@sandia.gov
Hewson, John	1532	jchewso@sandia.gov
Technical Library	01977	sanddocs@sandia.gov

Email—External [redacted]

Name	Company Email Address	Company Name
Nima Fathi	nfathi@unm.edu	The University of New Mexico

This page left blank

This page left blank